

THE MILKY WAY'S CIRCULAR VELOCITY CURVE BETWEEN 4 AND 14 KPC FROM APOGEE DATA

JO BOVY^{1,2}, CARLOS ALLENDE PRIETO^{3,4}, TIMOTHY C. BEERS^{5,6}, DMITRY BIZYAEV⁷, LUIZ N. DA COSTA^{8,9}, KATIA CUNHA^{9,10}, GARRETT L. EBELKE⁷, DANIEL J. EISENSTEIN¹¹, PETER M. FRINCHABOV¹², ANA ELIA GARCÍA PÉREZ¹³, LÉO GIRARDI^{8,14}, FRED R. HEARTY¹³, DAVID W. HOGG^{15,16}, JON HOLTZMAN¹⁷, MARCIO A. G. MAIA^{8,9}, STEVEN R. MAJEWSKI¹³, ELENA MALANUSHENKO⁷, VIKTOR MALANUSHENKO⁷, SZabolcs MÉSZÁROS^{3,4}, DAVID L. NIDEVER¹³, ROBERT W. O'CONNELL¹³, CHRISTINE O'DONNELL¹³, AUDREY ORAVETZ⁷, KAIKE PAN⁷, HELIO J. ROCHA-PINTO^{8,18}, RICARDO P. SCHIAVON¹⁹, DONALD P. SCHNEIDER^{20,21}, MATHIAS SCHULTHEIS²², MICHAEL SKRUTSKIE¹³, VERNE V. SMITH^{5,9}, DAVID H. WEINBERG²³, JOHN C. WILSON¹³, AND GAIL ZASOWSKI^{13,23}

ABSTRACT

We measure the Milky Way's rotation curve over the Galactocentric range $4 \text{ kpc} \lesssim R \lesssim 14 \text{ kpc}$ from the first year of data from the Apache Point Observatory Galactic Evolution Experiment (APOGEE). We model the line-of-sight velocities of 3,365 stars in fourteen fields with $b = 0^\circ$ between $30^\circ \leq l \leq 210^\circ$ out to distances of 10 kpc using an axisymmetric kinematical model that includes a correction for the asymmetric drift of the warm tracer population ($\sigma_R \approx 35 \text{ km s}^{-1}$). We determine the local value of the circular velocity to be $V_c(R_0) = 218 \pm 6 \text{ km s}^{-1}$ and find that the rotation curve is approximately flat with a local derivative between $-3.0 \text{ km s}^{-1} \text{ kpc}^{-1}$ and $0.4 \text{ km s}^{-1} \text{ kpc}^{-1}$. We also measure the Sun's position and velocity in the Galactocentric rest frame, finding the distance to the Galactic center to be $8 \text{ kpc} < R_0 < 9 \text{ kpc}$, radial velocity $V_{R,\odot} = -10 \pm 1 \text{ km s}^{-1}$, and rotational velocity $V_{\phi,\odot} = 242^{+10}_{-3} \text{ km s}^{-1}$, in good agreement with local measurements of the Sun's radial velocity and with the observed proper motion of Sgr A*. We investigate various systematic uncertainties and find that these are limited to offsets at the percent level, $\sim 2 \text{ km s}^{-1}$ in V_c . Marginalizing over all the systematics that we consider, we find that $V_c(R_0) < 235 \text{ km s}^{-1}$ at $> 99\%$ confidence. We find an offset between the Sun's rotational velocity and the local circular velocity of $26 \pm 3 \text{ km s}^{-1}$, which is larger than the locally-measured solar motion of 12 km s^{-1} . This larger offset reconciles our value for V_c with recent claims that $V_c \gtrsim 240 \text{ km s}^{-1}$. Combining our results with other data, we find that the Milky Way's dark-halo mass within the virial radius is $\sim 8 \times 10^{11} M_\odot$.

Subject headings: Galaxy: disk — Galaxy: fundamental parameters — Galaxy: general — Galaxy: kinematics and dynamics — Galaxy: structure — stars: kinematics

¹ Institute for Advanced Study, Einstein Drive, Princeton, NJ 08540, USA; bovy@ias.edu

² Hubble fellow

³ Instituto de Astrofísica de Canarias (IAC), E-38200 La Laguna, Tenerife, Spain

⁴ Departamento de Astrofísica, Universidad de La Laguna (ULL), E-38206 La Laguna, Tenerife, Spain

⁵ National Optical Astronomy Observatory, Tucson, AZ 85719, USA

⁶ Department of Physics & Astronomy and JINA (Joint Institute for Nuclear Astrophysics), Michigan State University, East Lansing, MI 48824, USA

⁷ Apache Point Observatory, P.O. Box 59, Sunspot, NM 88349, USA

⁸ Laboratório Interinstitucional de e-Astronomia - LIneA, Rua Gal. José Cristino 77, Rio de Janeiro, RJ - 20921-400, Brazil

⁹ Observatório Nacional, Rio de Janeiro, RJ 20921-400, Brazil

¹⁰ Steward Observatory, U. Arizona, Tucson, AZ 85719, USA

¹¹ Harvard-Smithsonian Center for Astrophysics, 60 Garden St., MS #20, Cambridge, MA 02138, USA

¹² Department of Physics and Astronomy, Texas Christian University, Fort Worth, TX 76129, USA

¹³ Department of Astronomy, University of Virginia, Charlottesville, VA, 22904, USA

¹⁴ Osservatorio Astronomico di Padova - INAF, Vicolo dell'Osservatorio 5, I-35122 Padova, Italy

¹⁵ Center for Cosmology and Particle Physics, Department of Physics, New York University, 4 Washington Place, New York, NY 10003, USA

¹⁶ Max-Planck-Institut für Astronomie, Königstuhl 17, D-69117 Heidelberg, Germany

¹⁷ New Mexico State University, Las Cruces, NM 88003, USA

¹⁸ Observatório do Valongo, Universidade Federal do Rio de Janeiro, Rio de Janeiro RJ 20080-090, Brazil

¹⁹ Gemini Observatory, 670 A'ohoku Place, Hilo, HI 96720, USA

²⁰ Department of Astronomy and Astrophysics, The Pennsylvania State University, University Park, PA 16802, USA

²¹ Institute for Gravitation and the Cosmos, The Pennsylvania State University, University Park, PA 16802, USA

²² Institut Utinam, CNRS UMR6213, OSU THETA, Université de Franche-Comté, 41bis, avenue de l'Observatoire , 25000 Besançon, France

²³ The Ohio State University, Department of Astronomy, Columbus OH 43210, USA

1. INTRODUCTION

The Milky Way's inner rotation curve $V_c(R)$, and in particular its value $V_c \equiv V_c(R_0)$ at the Sun's Galactocentric radius R_0 , is crucial for our understanding of many Galactic and extra-galactic observations. It provides an important constraint on mass models for the Milky Way and the question of whether the Galactic disk is maximal. The shape of the rotation curve is an important ingredient for realistic models of the disk's formation and evolution. The circular velocity at the Sun, which is located approximately 2.5 disk scale lengths from the Galactic center (Bovy et al. 2012b), is also important for placing the Milky Way in a cosmological context, for example, when asking whether the Milky Way follows the Tully-Fisher relation (e.g., Klypin, Zhao, & Somerville 2002; Flynn et al. 2006; Hammer et al. 2007). V_c is often considered to be an important parameter for dark-matter direct-detection experiments and for correcting the motion of extra-galactic objects for the motion of the Sun, although we seek to dispel these notions below (§ 5.3).

Traditionally, the local circular velocity has been obtained by measuring the Sun's motion with respect to an object that is assumed to be at rest with respect to the Galaxy. The most robust of those measurements is that derived from the observed proper motion of Sgr A* (Reid & Brunthaler 2004), even though this requires an estimate of R_0 . An alternative method that does not require knowledge of R_0 consists of measuring the Sun's reflex motion using a stellar tidal stream with orbital pole near $l = 270^\circ$ (Majewski et al. 2006). Similar measurements using samples of halo stars (Sirko et al. 2004), or the globular cluster system (Woltjer 1975), may be contaminated by the residual, presumably prograde, motion of these populations and, thus, only provide a lower limit. As discussed in detail in § 5.3, such measurements intrinsically measure the Sun's rotational velocity, $V_{\phi,\odot}$, rather than the circular velocity. To arrive at V_c , these measurements depend on a highly uncertain correction for the Sun's motion with respect to V_c . The measurement of V_c by observing the extreme line-of-sight velocity of HI emission toward Galactic longitudes $l \sim 90^\circ$ in principle also directly measures $V_{\phi,\odot}$ (Knapp et al. 1979), although the HI density drops too steeply with radius for $V_{\phi,\odot}$ to be directly observed, and more intricate modeling is necessary to turn the HI emission toward $l \sim 90^\circ$ into a constraint on V_c .

Other measurements of V_c have in the past been limited to measurements of the Oort constants, due to a lack of data at large distances from the Sun (e.g., Feast & Whitelock 1997). Recently, new estimates have been obtained from the kinematics of masers in the Galactic disk (Reid et al. 2009; Bovy et al. 2009a; McMillan & Binney 2010), and from fitting an orbit to the cold stellar stream GD-1 (Koposov et al. 2010). However, until now, no consensus has been reached as to whether V_c lies near the IAU-recommended value of $V_c = 220 \text{ km s}^{-1}$ (Kerr & Lynden-Bell 1986), or whether it needs to be revised upward to around $V_c = 250 \text{ km s}^{-1}$ (e.g., Ghez et al. 2008; Reid et al. 2009; Bovy et al. 2009a; Schönrich 2012).

Most of the information relating to the shape of the rotation curve is based upon the observed kinematics of the HI emission, either through the tangent-point

method at $l < 90^\circ$ and $l > 270^\circ$ (van de Hulst et al. 1954; Gunn et al. 1979; Levine et al. 2008), or through the observed thickness of the HI layer at $90^\circ < l < 270^\circ$ (Merrifield 1992). Such measurements are purely geometrical and, in particular, cannot constrain the component of Galactic rotation that has a uniform angular speed. This also holds for measurements of V_c based on the line-of-sight velocities of open clusters (e.g., Frinchaboy 2008). The best constraints on the local slope of the circular-velocity curve therefore also come from measurements of the Oort constants (e.g., Feast & Whitelock 1997), although the HI observations are crucial to measuring the rotation curve over the full radial range of the disk.

In this paper we present the first measurement of the Milky Way's circular velocity curve using kinematically-warm stellar tracers out to heliocentric distances of 10 kpc, from the Sloan Digital Sky Survey III's Apache Point Observatory Galactic Evolution Experiment (SDSS-III/APOGEE; Eisenstein et al. 2011; S. R. Majewski, et al. 2012, in preparation). APOGEE is a high-resolution spectroscopic survey covering all of the major components of the Galaxy that—crucially—operates in the near-infrared, which allows stars to be observed to large distances in the dust-obscured regions of the inner Milky Way disk. While warm stellar-disk tracers do not on average rotate at the circular velocity like the HI emission discussed above, their offset from $V_c(R)$ —the so-called asymmetric drift (Strömgren 1946)—is a dynamical effect that can be calculated from their observed velocity dispersion. Because our measurement relies on a dynamical effect, we are sensitive to V_c in the sense of the radial-force component at R , rather than to $V_{\phi,\odot}$, although the large range in l of our sample allows us to independently measure $V_{\phi,\odot}$. Additional benefits of using the intermediate-age to old stellar population to trace the dynamics of the disk are that these populations are much less sensitive to non-axisymmetric streaming motions than cold gas, and that the large asymmetric drift can be used to constrain the component of Galactic rotation that possesses a uniform angular speed.

Using a data set of 3,365 stars at $b = 0^\circ$ along 14 lines of sight covering $30^\circ \leq l \leq 210^\circ$, we find that the Milky Way's rotation curve is approximately flat over $4 \text{ kpc} < R < 14 \text{ kpc}$, with $V_c(R_0) = 218 \pm 6 \text{ km s}^{-1}$. A value of $V_c > 235 \text{ km s}^{-1}$ is ruled out at $> 99\%$ confidence by our data. Our measurement of $V_{\phi,\odot} = 242^{+10}_{-3} \text{ km s}^{-1}$ agrees with the observed proper motion of Sgr A*, but the Sun's offset from V_c is larger than the locally-measured value (Schönrich et al. 2010) by $14 \pm 3 \text{ km s}^{-1}$.

The outline of this paper is as follows. In § 2, we describe the APOGEE data set. The methodology employed to model the observed kinematics of the kinematically-warm tracer population is presented in § 3. We discuss our results in § 4, including a detailed discussion of potential systematics in § 4.2. The influence of non-axisymmetric streaming motions on our data is assessed in § 5.1. We compare our new measurement of $V_c(R)$ with previous determinations in § 5.2. In § 5.3, we discuss the implications of our measurement of the Sun's offset from circular motion and, in § 5.4, we estimate the mass of the Milky Way implied by our data, as well as other recent data. We conclude in § 6. Appendix A

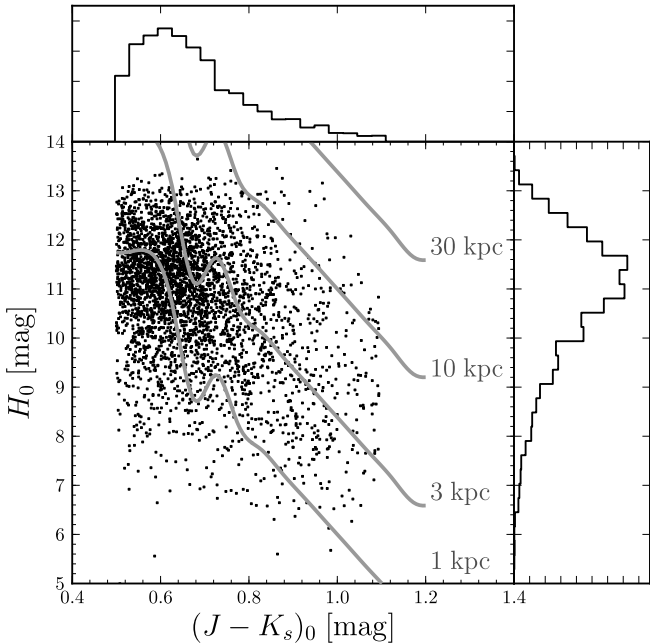


FIG. 1.— Distribution of the 3,365 mid-plane data points in extinction-corrected color and magnitude. The gray curves give approximate distances based on the peak of the distance likelihood in FIG. 11.

describes how photometric distances for the stars in our sample are estimated. In Appendix B we discuss extensive mock-data tests used to test our methodology and to determine the data’s sensitivity to $V_c(R)$. In what follows we sometimes refer to the circular velocity at the Sun’s location $V_c(R_0)$ by the shorthand notation V_c .

2. APOGEE DATA

The SDSS-III/APOGEE is a near-infrared (NIR; H -band; 1.51 to 1.70 μm), high-resolution ($R \approx 22,500$), spectroscopic survey, targeting primarily red giants in all Galactic environments, with emphasis on the disk and the bulge. The APOGEE instrument (Wilson et al. 2010, J. Wilson et al. 2012, in preparation) consists of a spectrograph with 300 2” fibers that reaches a signal-to-noise ratio of 100 per pixel (at about Nyquist sampling) at $H \leq 12.2$ in three one-hour visits during bright time on the 2.5-meter Sloan telescope, at the Apache Point Observatory in Sunspot, NM (Gunn et al. 2006). A detailed account of the target selection and data reduction pipeline is given in G. Zasowski et al. 2012 (in preparation) and D. Nidever et al. 2012 (in preparation), respectively. Here we summarize the, for our purposes, most important aspects of the target selection and data reduction.

Our analysis is based on data from APOGEE’s first year of regular survey operations (09-11-2011 to 05-07-2012). We use data from fields centered on $b = 0^\circ$; APOGEE fields have a radius of 1.5° . By only selecting fields with $30^\circ \leq l \leq 330^\circ$ we avoid the bulge region. We resolve multiple visits to the same field by choosing the highest signal-to-noise ratio measurement of the Doppler shift, rather than combining the multiple epochs, because the typical uncertainty in the line-of-sight velocity is well below 1 km s^{-1} . Only primary survey targets

are selected, excluding targets flagged as possible cluster members and stars observed as part of any of various special programs. We exclude stars with $(J - K_s)_0 > 1.1$, as these are problematic for the isochrone model we adopt to marginalize over their distances (see Appendix A). The resulting sample has 3,365 stars in 14 different fields with $30^\circ \leq l \leq 210^\circ$. The distribution of the data in extinction-corrected color and magnitude is shown in FIG. 1 and the distribution of the stars on the sky is shown in FIG. 2. The properties of the sample in the various fields are given in TABLE 1.

Spectroscopic targets are selected from the 2MASS point-source catalog (Skrutskie et al. 2006), with the following quality restrictions applied: photometric uncertainties less than 0.1 mag in J , H , and K_s ; quality flag ‘A’ or ‘B’ in JHK_s ; nearest neighbor more than 6” away; confusion flag ‘0’ for JHK_s ; galaxy contamination flag ‘0’; read flag ‘1’ or ‘2’ for JHK_s ; extkey equal to -1 . The extinction corrections for targets in the Galactic mid-plane use mid-IR photometry from either WISE (Wright et al. 2010) or Spitzer-IRAC GLIMPSE-I (Churchwell et al. 2009); therefore, both mid-IR detections and mid-IR photometric uncertainties less than 0.1 mag are required²⁴. APOGEE’s magnitude range— $7 \leq H < 13.8$ —is within the completeness limits for both the IRAC and WISE surveys. Photometry for all targets is extinction-corrected using the Rayleigh Jeans Color Excess method (RJCE; Majewski et al. 2011), which provides extinction values A_K with typical random uncertainties $\lesssim 0.05$ mag for individual stars using a combination of near- and mid-IR photometry. Variations in the adopted extinction law among different lines of sight can lead to differences of up to 7% (Zasowski et al. 2009).

The color range that we select, $0.5 \leq (J - K_s)_0 \leq 1.1$, includes the red clump ($(J - K_s)_0 = 0.5$ to 0.7) and the red giant branch, for all metallicities. Dwarf contamination is most severe at $(J - K_s)_0 < 0.8$, with most redder dwarfs being faint M and brown dwarfs. Most APOGEE observations consist of three or more individual “visits”, with only three visits for stars with $7 \leq H < 12.2$, and six visits for $12.2 \leq H < 12.8$. About 10% of our sample consists of even more visits for stars with $12.8 \leq H < 13.8$. The APOGEE sampling is random in color, and a combination of random and systematic in apparent magnitude (selecting every N -th star in a magnitude-ordered list for each field); details of the selection function are unimportant for our purposes and it suffices to note that the spectroscopic sample is a representative sample of the underlying (non-extinction-corrected) magnitude distribution. At $H < 11$, dwarf contamination in the APOGEE fields is expected to be less than 10% based on population-synthesis models (Girardi et al. 2005) in the APOGEE fields (L. Girardi, 2012, in preparation). Models predict that this contamination increases to about 20% at $11 < H < 12$. We explicitly include dwarf contamination as a free parameter in the analysis below.

Line-of-sight velocities are determined for each individual visit by cross-correlating against a set of ≈ 100 syn-

²⁴ The first version of the APOGEE target selection did not consistently insist on the availability of extinction corrections, such that a small number of mid-plane targets do not have extinction estimates. We have removed 17 stars without extinction estimates from the sample.

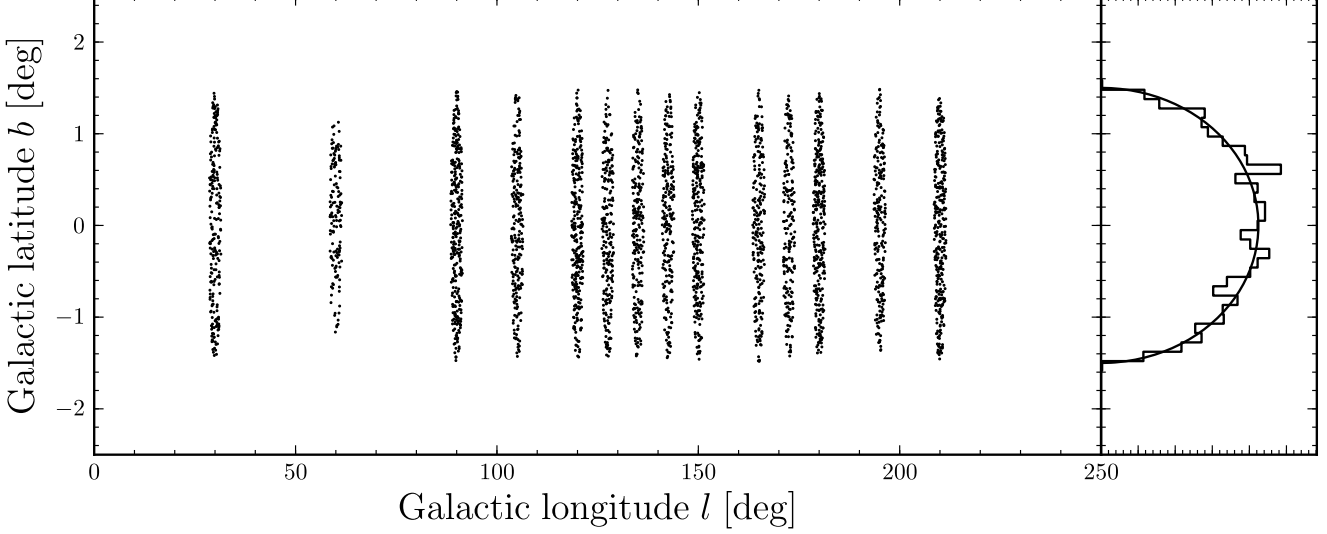


FIG. 2.— Distribution of the data in (l, b) . The smooth curve in the right panel is a uniform distribution in (l, b) over each field.

TABLE 1
PROPERTIES OF THE SAMPLE

Field location l [degrees]	Stars	$H < 12.2$	$12.2 \leq H < 12.8$	$12.8 \leq H < 13.8$	median	A_K
30°	230	108		33	89	0.8
60°	141	50		33	58	0.6
90°	310	178		46	86	0.4
105°	222	222		0	0	0.2
120°	289	157		84	48	0.3
127°	228	228		0	0	0.3
135°	229	229		0	0	0.3
142°	227	227		0	0	0.6
150°	279	150		87	42	0.3
165°	225	225		0	0	0.1
172°	199	199		0	0	0.3
180°	314	174		90	50	0.2
195°	227	227		0	0	0.2
210°	315	173		91	51	0.2

thetic template spectra that sparsely cover the stellar-parameter range $3,500 \text{ K} < T_{\text{eff}} < 25,000 \text{ K}$ in effective temperature, T_{eff} , $-2 < [\text{Fe}/\text{H}] < 0.3$ in metallicity, $[\text{Fe}/\text{H}]$, and $2 < \log g < 5$ in surface gravity, $\log g$ (see D. Nidever et al. 2012, in preparation, for details on the exact procedure). The distribution of rms scatter in the measured line-of-sight velocity for stars with multiple observations peaks around 0.1 km s^{-1} . Tests of field-to-field variations indicate that the zero point of the velocity scale is stable at the 0.05 km s^{-1} level. A preliminary comparison between the APOGEE-measured and literature line-of-sight velocity of 53 stars in M3, M13, and M15 shows that the APOGEE zeropoint accuracy is $\approx 0.26 \pm 0.20 \text{ km s}^{-1}$ (see D. Nidever et al., 2012, in preparation for full details). In what follows we ignore the uncertainties on the line-of-sight velocities entirely (that is, we assume that they are zero), because the uncertainties are much smaller than any velocity difference that we could hope to measure with our sample of $\approx 3,000$ stars having a typical dispersion of $\approx 35 \text{ km s}^{-1}$.

Repeated visits to the same star will eventually allow binary stars to be flagged as such based on the variability

of their line-of-sight velocities. However, currently multiple visits are not available for all 14 APOGEE fields that we employ here, and removing fields without multiple visits would significantly reduce the longitudinal coverage of our sample. Using the stars in our sample that have multiple visits, we find that $\sim 4\%$ of stars show velocity variability at the 10 to 70 km s^{-1} level—the level at which they could be confused with the dispersion of a disk population. Binary contamination would spuriously increase the inferred velocity dispersion and therefore likely decrease the inferred circular velocity, due to the dispersion-dependence of the asymmetric-drift correction used below. However, as discussed below, the asymmetric drift for our sample is $\lesssim 6 \text{ km s}^{-1}$ at $R < 10 \text{ kpc}$, such that the effect of binary contamination on the velocity dispersion is $\ll 1 \text{ km s}^{-1}$. Therefore, we do not remove binaries from our sample, but we discuss the results obtained when removing them in § 4.2.

Stellar parameters and elemental abundances are determined by the APOGEE Stellar Parameters and Chemical Abundances Pipeline (ASPCAP; A. E. García Pérez et al., 2013, in preparation). After determining the

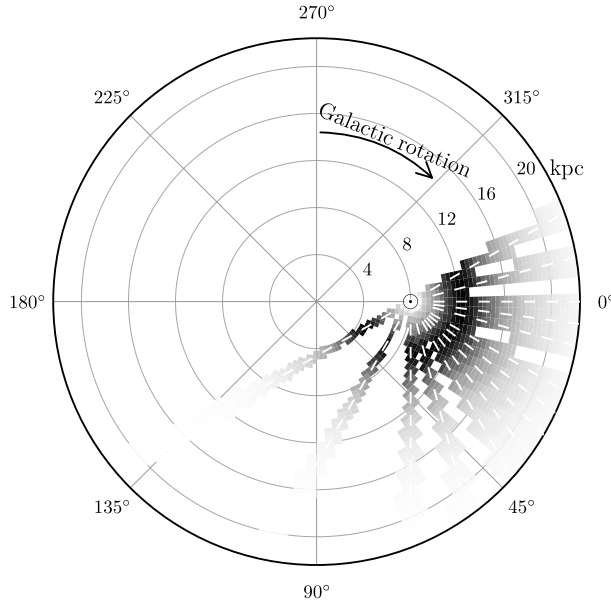


FIG. 3.— Sum of all photometric distance distributions $p(d|l, b, (J - K_s)_0, H_0, [\text{Fe}/\text{H}], \text{DF}, \text{iso})$ for stars in our sample, viewed from the north Galactic pole, with the Sun at azimuth 0° . These photometric-distance distributions are used in Equation (1) to marginalize over the distance to each individual star. We emphasize that this is *not* the underlying distance distribution of our sample, as individual distances are poorly constrained for the giants in our sample. The 14 fields that we use are indicated by dashed white lines.

spectral type, each star's microturbulence, T_{eff} , $[\text{Fe}/\text{H}]$, $\log g$, $[\alpha/\text{Fe}]$, $[\text{C}/\text{Fe}]$, and $[\text{N}/\text{Fe}]$ are determined through χ^2 minimization of the difference between the observed and synthetic spectra derived from ATLAS9 model-atmosphere grids (Kurucz 1979 and more recent updates). We only use $[\text{Fe}/\text{H}]$ in our analysis below, and in particular, we do *not* make use of $\log g$ for the purpose of selecting giants, because the measurement of $\log g$ has not been finalized yet within APOGEE. Preliminary comparisons with standard stars and globular clusters indicate that the metallicities are currently accurate, to a precision of ~ 0.1 dex at $[\text{Fe}/\text{H}] > -1$. All but 21 of the disk stars in our sample described below have higher metallicities than this, and all but 160 have $[\text{Fe}/\text{H}] > -0.5$.

Because many stars in our sample are on the red giant branch, and hence do not follow narrow magnitude-color relations like dwarfs and red clump stars, estimating precise distances to these stars is difficult. In what follows, we avoid estimating distances to the individual stars in our sample by marginalizing a kinematical model over the distance to the star. This marginalization is performed by integrating over the full photometric-distance probability distribution function (PDF) for each individual star, obtained from models for the stellar isochrones and initial mass function (IMF) of the giant stars in the sample, as well as a prior that the stars are in an exponential disk with a scale length of 3 kpc (Bovy et al. 2012c). This technique is discussed in detail in Appendix A. For dwarf stars, we assume that they are close enough that their distances are irrelevant for their kin-

matics. As such, we cannot show the spatial distribution of the stars in our sample. As an alternative, we show in FIG. 3 the sum of all of the photometric distance distributions for stars in our sample (assuming that they are all giants).

3. METHODOLOGY

3.1. General Considerations

Our approach to determining the Milky Way's rotation curve from the APOGEE data is to fit a kinematical, axisymmetric model to the observed line-of-sight velocities. In its most basic form, such a kinematical model consists of (a) a model for the rotation curve, (b) a model for the distribution of peculiar velocities with respect to circular motion as a function of Galactocentric radius, and (c) a set of parameters describing the transformation of positions and velocities from the heliocentric to the Galactocentric frame. These latter parameters are the distance R_0 from the Sun to the Galactic center, and the Sun's velocity with respect to the (dynamical) center of the Galaxy. We will ignore the small projection effects that arise at non-zero Galactic latitude and the vertical dependence of V_c , since these are all at the sub- km s^{-1} level for $|b| < 1.5^\circ$ and distances $\lesssim 10$ kpc (e.g., Bovy & Tremaine 2012). Therefore, we are only concerned with motions in the plane of the Galactic disk, and we ignore vertical motions.

The kinematical model provides the probability distribution of line-of-sight velocities as a function of position (Galactocentric radius R and azimuth ϕ , or distance d and Galactic longitude l), after marginalizing over the component of the velocity tangential to the line of sight. This requires knowing the distance, which is only weakly constrained for giants (see Appendix A). Therefore, we additionally marginalize the kinematical model over the distance to each star, to obtain the probability of the observed line-of-sight velocity of a star, given its position (l, b) , photometry $(J_0, H_0, K_{s,0})$, the iron abundance $[\text{Fe}/\text{H}]$ (taken as representative of the overall metallicity of the star), the kinematical model (represented by the circular-velocity curve $V_c(R)$ and the distribution of peculiar velocities, DF), and the coordinate-transformation parameters R_0 and $\mathbf{V}_\odot^{\text{gal}} = (V_{R,\odot}, V_{\phi,\odot})$ (where we label this parameter as “gal” to emphasize that this is the *full* velocity with respect to the center of the Galaxy, not just the Sun's motion with respect to the local circular velocity):

$$\begin{aligned}
 p(V_{\text{los}}|l, b, (J - K_s)_0, H_0, [\text{Fe}/\text{H}], V_c(R), R_0, V_{R,\odot}, V_{\phi,\odot}, \text{DF}, \text{iso}) \\
 = \sum_{\text{dwarf/giant}} P(\text{dwarf/giant}) \\
 \int dd p(V_{\text{los}}|d, l, b, V_c(R), R_0, V_{R,\odot}, V_{\phi,\odot}, \text{DF}) \\
 \times p(d|l, b, (J - K_s)_0, H_0, [\text{Fe}/\text{H}], \text{DF}, \text{iso}, \text{dwarf/giant}). \tag{1}
 \end{aligned}$$

The first factor within the integral is produced by marginalizing the kinematical model over the velocity component tangential to the line of sight at a given position. The second factor is given by the photometric-distance PDF, discussed in Appendix A; we include ‘iso’ in the prior information to emphasize

that we use an isochrone and IMF model to obtain the photometric-distance PDFs. We also marginalize over whether a star is a giant or a dwarf star, which changes the photometric-distance PDF; the dwarf contamination probability $P(\text{dwarf})$ is a single free parameter in our model. Equation (1) is the likelihood for a single star, and the total likelihood for the sample is calculated by multiplying together the individual likelihoods for all the 3,365 data points. This total likelihood is what we optimize to fit models to the data.

We can also calculate the distribution of line-of-sight velocities for individual fields, which we will use later to show comparisons between the best-fit model and the data. For the distribution of V_{los} of a field centered at $(l_{\text{field}}, b_{\text{field}})$ we obtain

$$\begin{aligned} p(V_{\text{los}}|l_{\text{field}}, b_{\text{field}}, V_c(R), R_0, V_{R,\odot}, V_{\phi,\odot}, \text{DF, iso}) \\ = \int dl db \int d(J - K_s)_0 dH_0 d[\text{Fe}/\text{H}] \\ p((J - K_s)_0, H_0, [\text{Fe}/\text{H}], l, b|l_{\text{field}}, b_{\text{field}}, \text{DF, iso}) \\ \times \int dd p(V_{\text{los}}|l, b, (J - K_s)_0, H_0, [\text{Fe}/\text{H}], V_c(R), R_0, \\ V_{R,\odot}, V_{\phi,\odot}, \text{DF, iso}), \end{aligned} \quad (2)$$

where $p(J - K_s, H, [\text{Fe}/\text{H}], l, b|l_{\text{field}}, b_{\text{field}}, \text{DF, iso})$ is taken directly from the field's data (that is, we sum over the data $(l, b, (J - K_s)_0, H_0, [\text{Fe}/\text{H}])$).

3.2. Kinematical Model

We now describe in detail the full model that is fit to the data. Our fiducial model for the distribution of velocities in the Galactocentric rest frame is that it is a single biaxial Gaussian, with a mean radial velocity of zero because of the assumption of axisymmetry, and a mean rotational velocity given by the local circular velocity $V_c(R)$, adjusted for the local asymmetric drift $V_a(R; \sigma_R, h_R, h_\sigma)$, which is a function of the velocity dispersion, σ_R , and the radial and radial-velocity dispersion scale lengths of the population (h_R and h_σ , respectively, see below). The only free parameters of the distribution of peculiar velocities are therefore the radial and rotational velocity dispersions, as the mixed radial–azimuthal moment vanishes, again because of the assumption of axisymmetry. The mixed moment, or equivalently the vertex deviation, in the solar neighborhood does not vanish for the warm disk population (Dehnen & Binney 1998), but this seems likely to result from the presence of moving groups, and not from the smooth underlying distribution having a strong non-zero vertex deviation (Bovy et al. 2009b).

Assuming that the distribution of velocities in the Galactocentric cylindrical frame is Gaussian allows us to analytically marginalize the velocity distribution over the velocity component tangential to the line of sight. The resulting one-dimensional distribution is itself Gaussian, with mean $(V_c(R) - V_a(R; \sigma, h_R, h_\sigma)) \sin(\phi + l)$ and variance $\sigma_R^2 (1 + \sin^2(\phi + l) (X^2 - 1))$, where X^2 is the ratio of the rotational and radial velocity variances $X^2 \equiv \sigma_\phi^2 / \sigma_R^2$. The Galactocentric line-of-sight velocity for a star is calculated from its heliocentric line-of-sight

velocity

$$V_{\text{los}}^{\text{gal}} = V_{\text{los}}^{\text{helio}} - V_{R,\odot} \cos l + \Omega_\odot R_0 \sin l, \quad (3)$$

where we have written the Sun's velocity in terms of its angular velocity Ω_\odot . This angular velocity is expected to be close to the observed proper motion of Sgr A* in the plane of the Galaxy (30.24 km s⁻¹ kpc⁻¹; Reid & Brunthaler 2004), but we leave it as a free parameter, in addition to $V_{R,\odot}$.

The asymmetric drift in the plane of the Galaxy of a population of stars is given by (e.g., Binney & Tremaine 2008)

$$\frac{V_c(R)V_a(R)}{\sigma_R^2(R)} = \frac{1}{2} \left[X^2 - 1 - \frac{\partial \ln(\nu_* \sigma_R^2)}{\partial \ln R} \right], \quad (4)$$

assuming that the radial–vertical velocity moment $\sigma_{RZ} = 0$ in the Galactic plane, for symmetry reasons. For an exponential-disk tracer population (stellar tracer density $\nu_* \propto e^{-R/h_R}$) with an exponentially declining radial-velocity dispersion ($\sigma_R(R) \propto e^{-R/h_\sigma}$), this formula becomes

$$\frac{V_c(R)V_a(R)}{\sigma_R^2(R)} = \frac{1}{2} \left[X^2 - 1 + R \left(\frac{1}{h_R} + \frac{2}{h_\sigma} \right) \right]. \quad (5)$$

The main unknown in this relation is X^2 and its dependence on R . In the fit below, we assume a constant X^2 with R for calculating the model's Gaussian line-of-sight velocity dispersion (see above), but to model the asymmetric drift more realistically, we use an $X^2(R)$ coming from an axisymmetric equilibrium model for the distribution function $f(E, L)$ in a disk with a constant circular velocity with radius. For this distribution function, we use a Dehnen distribution function (Dehnen 1999) given by

$$f_{\text{Dehnen}}(E, L) \propto \frac{\nu_*(R_e)}{\sigma_R^2(R_e)} \exp \left[\frac{\Omega(R_e) [L - L_c(E)]}{\sigma_R^2(R_e)} \right], \quad (6)$$

where R_e , L_c , and $\Omega(R_e)$ are the radius, angular momentum, and angular velocity, respectively, of the circular orbit with energy E . Using the procedure given in § 3.2 of Dehnen (1999), we choose the $\nu_*(R)$ and $\sigma_R(R)$ functions such that they reproduce a disk with exponential surface density and velocity-dispersion profiles to an accuracy of a fraction of a percent at all radii.

The asymmetric drift for the Dehnen distribution function (DF) for a population with $\sigma_R(R_0) = 0.2 V_c(R_0) \approx 44$ km s⁻¹ is shown in FIG. 4 for $h_R = 3$ kpc, $h_\sigma = 8$ kpc. The same is shown for a population with $\sigma_R(R_0) = 0.1 V_c(R_0) \approx 22$ km s⁻¹, and the difference, normalized for the difference in σ_R between them, is small. For different values of h_R and h_σ we correct this function using Equation (5). As different values for h_R and h_σ lead to a different $X^2(R)$, this approach is slightly incorrect, but tests show that the difference in V_a is $\lesssim 5\%$ for reasonable values of h_R and h_σ . As the asymmetric drift is typically $\lesssim 20$ km s⁻¹ for our sample, this leads to changes $\lesssim 1$ km s⁻¹, which we can ignore. Similarly, differences in X^2 for our sample from this model are typically $\lesssim 0.2$, also leading to changes $\lesssim 1$ km s⁻¹, such that our assumption of a constant $X^2(R)$ does not strongly bias the value of the

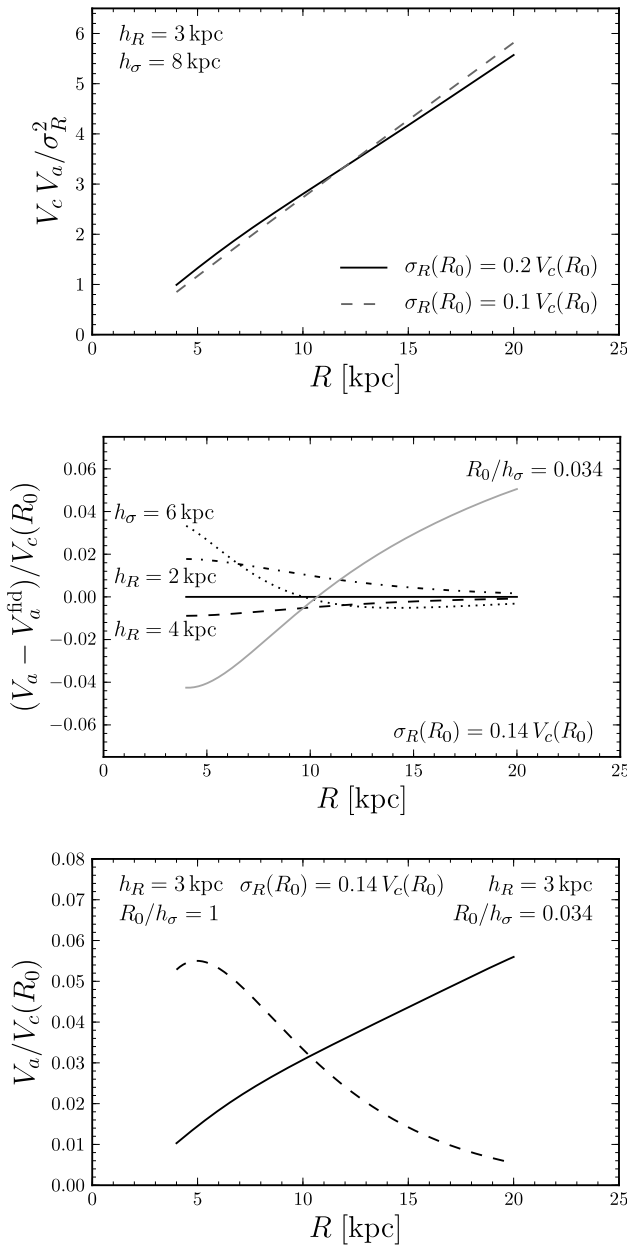


FIG. 4.— Asymmetric-drift model used in this paper. The top panel shows the asymmetric drift V_a in a Dehnen DF (Equation [6]), expressed dimensionlessly as $V_c V_a / \sigma_R^2$. We use the $\sigma_R(R_0) = 0.2V_c(R_0)$ curve and show the $\sigma_R(R_0) = 0.1V_c(R_0)$ for comparison. The middle panel shows the difference in asymmetric drift for different values of h_R and h_σ , using the solid curve from the top panel as the fiducial model. The bottom panel shows the actual asymmetric-drift correction as a fraction of the circular velocity used for the best-fit model below (solid line), and also shows the correction for $R_0/h_\sigma = 1$ (dashed line). All curves in the middle and bottom panels have $\sigma_R(R_0) = 0.14V_c(R_0)$ (the best-fit value for the APOGEE sample, see below).

inferred circular velocity. In the exponential-disk model, the asymmetric drift for our sample is $\lesssim 25$ km s $^{-1}$ at all radii, even in the innermost disk (Freeman 1987).

The middle panel of FIG. 4—now for $\sigma_R(R_0) = 0.14V_c$, the best-fit value below—shows the difference in asymmetric drift for different values of h_R and h_σ ; the main difference is at small R . This figure shows that

the dependence of the asymmetric drift correction on h_R and h_σ at R_0 is mostly $\lesssim 0.02 V_c$ —as it is unlikely that the scale length is as small as 2 kpc for this sample of stars (Bovy et al. 2012c), or that the radial-velocity dispersion scale length is much shorter than 8 kpc—which is the same as the statistical uncertainty on the circular velocity that we infer below. Therefore, the systematic uncertainty due to the scale length of the population of stars is $\lesssim 4$ km s $^{-1}$ at R_0 , and likely $\lesssim 2$ km s $^{-1}$. We could directly measure the scale length of our sample, but as this requires a detailed understanding of the dust distribution in the plane of the Galaxy, and as it does not contribute greatly to the error budget of our measurement, we do not attempt it here.

Our best-fit model below has a radial velocity dispersion that is approximately flat over the range in R considered here. In this case, the asymmetric-drift correction increases with R , as is clear from Equation (5), and the difference between this dispersion profile and that considered above is shown in the middle panel of FIG. 4. The bottom panel of FIG. 4 shows the actual asymmetric-drift correction applied in our best-fit model below. It is clear that this correction is small ($\lesssim 6$ km s $^{-1}$ at $R < 10$ kpc); hence it does not drive our inferred value for V_c below. The bottom panel of FIG. 4 also illustrates that, if the dispersion scale length were smaller than that in our best-fit model below, then the circular velocity curve would drop more steeply than what we infer below.

In addition to the kinematical model discussed so far, we include an outlier model that consists of a Gaussian with a width of $\sigma = 100$ km s $^{-1}$, centered on a mean value that is a free parameter in the model. This outlier model exists primarily to deal with data-processing outliers, stars with a color and magnitude that places them beyond the disk, and close binaries with large velocity amplitudes (as we do not currently have a sufficient number of APOGEE epochs for each star to confidently remove these from the sample). In all of the fits below, the outlier fraction is $\lesssim 1\%$, thus it does not influence our fits.

3.3. Dwarf Contamination

The dwarf contribution to the likelihood in Equation (1) could in principle be treated in the same way as the giant contribution, by integrating over the $p(d|l, b, (J - K_s)_0, H_0, [\text{Fe}/\text{H}], \text{DF}, \text{iso}, \text{dwarf})$ obtained from a similar isochrone and IMF model as for the giants. However, this is problematic, because the main sequence is much narrower than the giant branch, such that this integral is dominated by a narrow range of distances. As all of the dwarfs in our sample are faint main-sequence stars, they are expected to all be within a few 100 pc from the Sun, and thus be relatively unaffected by the radial and azimuthal gradients in velocity distribution that we model for the giant stars. Our approach is therefore to replace the integration over distance with a single evaluation at zero distance from the Sun for the dwarf part of the likelihood. The dwarf stars are otherwise modeled using the same distribution of peculiar velocities as the giant stars, i.e., we assume that they are drawn from a similar population. The dwarf contamination in our best-fit model below is 7.5%, and is similar for other fits considered below. This is close to the value expected

from stellar-population-synthesis models (see § 2).

3.4. Mock Data Tests

The procedure described above makes non-trivial approximations to an ideal axisymmetric fit to the data. The most important of these is that, although we include the asymmetric drift as part of our model, we do not include the deviations from a Gaussian rotational-velocity distribution that are expected for a warm population of stars (with the same physical origin as the asymmetric drift). In addition to this assumption, we make small approximations to the full asymmetric drift expression in Equation (4). These simplifications are expected to have small effects on our analysis: The skew of the rotational-velocity distribution is only fully visible near the tangent point where the line-of-sight velocity is equal to the rotational velocity, but our sample covers a large range of distances for each line of sight, and 85% of our sample lies at $90^\circ < l < 270^\circ$, where there is no tangent point. As such, most stars are drawn from a distribution that is close to Gaussian.

To investigate these simplifications, we conduct a series of mock data tests. In these tests, we sample line-of-sight velocities from the best-fit flat-rotation-curve model below, except that we use the full Dehnen DF of Equation (6)—uncorrected, such that it does not quite reproduce the assumed exponential disk—rather than the Gaussian approximation used in the fit (we ignore the best-fit X^2 as the Dehnen DF has X^2 built-in). We then fit these mock data using the approximate methodology.

These mock data tests are described in detail in Appendix B. The results from these tests show that the approximations made in the analysis do not produce any significant bias in the fitted parameters. Fits with non-flat rotation curves to the mock data samples indicate that we can reliably determine the shape of the rotation curve between $4 \text{ kpc} < R < 14 \text{ kpc}$. The uncertainties in the fitted parameters for the mock data are approximately the same as those for the real data (see below), which indicates that the uncertainties in the Galactic parameters derived below for the real data are correct.

3.5. Parameter Sensitivity

We briefly discuss here how our data are sensitive to the parameters of the model. The mean heliocentric line-of-sight velocity at a position $(R, \phi) = (d, l)$ is given by (see Equation (3))

$$\bar{V}_{\text{los}} = \bar{V}_\phi \sin(\phi + l) + V_{R,\odot} \cos l - V_{\phi,\odot} \sin l, \quad (7)$$

where $\bar{V}_\phi = V_c - V_a$. We have treated the position and velocity of the Sun as free parameters, without imposing any prior on R_0 , and without assuming that the solar rotational velocity is given by the local circular velocity corrected for the (previously measured) velocity of the Sun with respect to the local standard of rest (LSR). We can determine the full space motion of the Sun from our sample, because the longitudinal dependence of the correction for the solar motion of the line-of-sight velocity of a star at $(R, \phi) \equiv (d, l)$ is sinusoidal ($\propto V_{\phi,\odot} \sin l$), while the dependence on the rotational velocity at the position of the star varies differently for the $d \approx 1$ to 10 kpc sample of APOGEE stars ($\propto (V_c - V_a) \sin(\phi + l)$). Mock data tests in Appendix B show that our sample

spans a sufficiently wide range in Galactic longitude and distance to disentangle these two effects, and measure the solar Galactocentric motion. Because we know the Sun’s rotational frequency from assuming that the radio source Sgr A* at the Galactic center is at rest with respect to the disk, we have an independent check on our inferred value for the solar motion (but *we do not use the measured proper motion of Sgr A* as a prior on the solar motion*).

We can then turn a measurement of $\bar{V}_\phi(R)$ into a measurement of $V_c(R)$ by correcting for the asymmetric drift, $V_a(R)$, using Equation (5). This transformation requires a measurement, foremost, of the radial-velocity dispersion, $\sigma_R(R)$. We can measure σ_R almost directly using the $l = 180^\circ$ line of sight. By modeling $\sigma_R(R)$ as an exponential and assuming a constant σ_ϕ^2/σ_R^2 , we can measure $\sigma_R(R)$ from the line-of-sight-velocity dispersion at each l . The only subtlety here is that, in the first quadrant ($R < R_0, l < 90^\circ$), we typically sample positions where V_{los} is close to V_ϕ , while in the second and third quadrants ($R > R_0, 90^\circ < l < 270^\circ$), V_{los} is mainly composed of V_R . We can then use the measurement of $\sigma_R(R)$ to correct for V_a and derive V_c .

The fact that our data sample is composed of the intermediate-age to old disk population is crucial for our ability to measure the full shape of the rotation curve. Traditional tangent-point analyses of the HI emission at $l < 90^\circ$, or the measurement of $V_c(R)$ at $90^\circ < l < 270^\circ$ using the thickness of the HI layer, are insensitive to solid-body (uniform angular speed) contributions to the rotation curve, because these do not give rise to line-of-sight velocities for circular orbits. Formally, the HI velocities are invariant under the transformation $V_c(R) \rightarrow V_c(R) + \Omega R$. However, this is not the case for a warm tracer population, as, for example, the mean rotational velocity transforms as

$$\bar{V}_{\text{los}} \rightarrow \bar{V}_{\text{los}} + V_a(\Omega_0) \left(1 - \frac{1}{1 + \Omega/\Omega_0(R)} \right) \sin(\phi + l). \quad (8)$$

where $\Omega_0(R) = V_c(R)/R$. Thus, the addition of ΩR to $V_c(R)$ changes \bar{V}_{los} by $\sim V_a \Omega/\Omega_0$, and $\Omega/\Omega_0 \sim 10\%$ gives rise to a few km s^{-1} changes in \bar{V}_{los} , which we can detect with our data. Equation (8) clearly shows that a warmer population, i.e., a population with a larger asymmetric drift, is *more sensitive* to the local slope of the rotation curve than a colder population.

4. RESULTS

4.1. Basic Models

In this section, we discuss the results from fitting the basic kinematical model of a single population with exponential $\nu_*(R)$ and $\sigma_R(R)$ profiles to the APOGEE disk mid-plane data from § 2. These are the main results of this paper. In a subsequent section, we discuss the effects of various systematics on these basic model fits, but we find in the end that they do not significantly bias the results for the Galactic parameters in this section.

The results from fitting a flat rotation curve to the APOGEE data are given in the left column of TABLE 2. The right column of this table gives the results when fitting a power-law model for the rotation curve $V_c(R) = V_c(R_0) (R/R_0)^\beta$. The best-fit power-law index

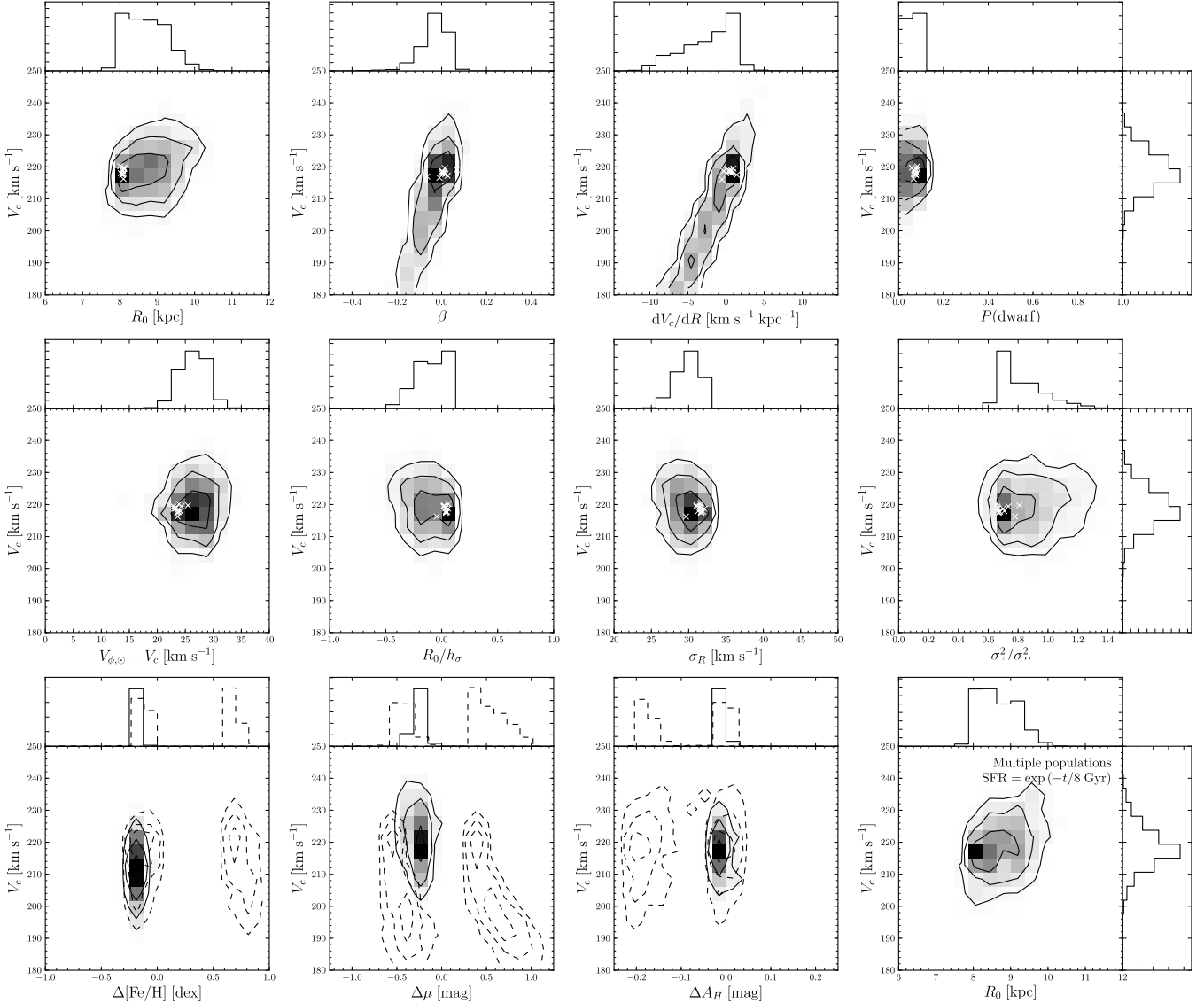


FIG. 5.— PDFs for the parameters of the model. All PDFs in the top two rows are for the model with a flat rotation curve, except for the middle two panels in the top row, which are for the power-law fit and the linear-polynomial fit. The top row has the (marginalized) joint PDF for V_c and (from left to right) R_0 , power-law index β , linear derivative dV_c/dR , and the dwarf contamination fraction $P(\text{dwarf})$. The middle row has (from left to right): the Sun’s peculiar rotational velocity $V_{\phi,\odot} - V_c$, the ratio of R_0 to the radial-dispersion scale length, the radial-velocity dispersion, and the ratio of tangential to radial-velocity dispersion squared. The bottom row explores various systematics: A systematic offset in $[\text{Fe}/\text{H}]$, in distance modulus μ , in extinction A_H , and using 20 populations between 1 and 10 Gyr with an exponentially-declining star-formation history and an increasing velocity dispersion as in Equation (11). In the leftmost three panels in the bottom row, the PDF for a single systematic offset is shown as the linear density and the solid contours, while the contours of the PDF when allowing for a different systematic offset in inner ($l \leq 90^\circ$) and outer ($l > 90^\circ$) fields are represented as dashed lines. The figures in the top two rows also include the best-fit result from leave-one-longitudinal-field-out fits to the data as white crosses (that is, leaving one of the 14 fields in TABLE 1 out of the data set).

in this case is approximately zero, such that both models for the rotation curve yield similar best-fit values for all parameters. The only significant difference between the two models for the rotation curve is the uncertainty interval for $V_c(R_0)$, which extends to lower values of V_c in the case of the power-law fit, although the upper limit on V_c stays approximately the same. We find that V_c is tightly constrained in the flat rotation-curve model: $V_c = 218 \pm 6 \text{ km s}^{-1}$ (68% confidence). When fitting a power law we find $V_c = 218^{+4}_{-19} \text{ km s}^{-1}$, with a strong correlation between the power-law index β (or, equivalently, the local derivative dV_c/dR of the circular ve-

locity with respect to R) and V_c . Other parameters do not exhibit any strong correlation with V_c (see discussion below).

When fitting a power-law model for the rotation curve, the local slope of the rotation curve is constrained to be $-3 \text{ km s}^{-1} \text{ kpc}^{-1} < dV_c/dR < 0.4 \text{ km s}^{-1} \text{ kpc}^{-1}$ (68% confidence), with a best-fit value near the upper end of that range, $0.2 \text{ km s}^{-1} \text{ kpc}^{-1}$. When fitting a linear model for the circular velocity the constraints are similar, and we do not discuss them further; the top, middle panels of FIG. 5 show the joint PDF for V_c and β (for the power-law fit) and dV_c/dR (for the lin-

TABLE 2
RESULTS FOR GALACTIC PARAMETERS AND TRACER PROPERTIES

Parameter	Flat rotation curve	Power-law $V_c(R) = V_c(R_0) (R/R_0)^\beta$
$V_c(R_0)$ [km s ⁻¹]	218±6	218^{+4}_{-19}
β	...	$0.01^{+0.01}_{-0.10}$
$dV_c/dR(R_0)$ [km s ⁻¹ kpc ⁻¹]	...	$0.2^{+0.2}_{-2.8}$
A [km s ⁻¹ kpc ⁻¹]	$13.5^{+0.2}_{-1.7}$	$13.5^{+0.2}_{-1.0}$
B [km s ⁻¹ kpc ⁻¹]	$-13.5^{+1.7}_{-0.2}$	$-13.7^{+3.3}_{-0.1}$
$(B^2 - A^2)/(2\pi G)$ [M _⊙ pc ⁻³]	...	$0.0002^{+0.0002}_{-0.0025}$
Ω_0 [km s ⁻¹ kpc ⁻¹]	$27.0^{+0.3}_{-3.5}$	$27.3^{+0.4}_{-4.2}$
R_0 [kpc]	$8.1^{+1.2}_{-0.1}$	$8.0^{+0.8}_{-0.1}$
$V_{R,\odot}$ [km s ⁻¹]	$-10.5^{+0.5}_{-0.8}$	$-10.3^{+1.1}_{-0.1}$
$V_{\phi,\odot}$ [km s ⁻¹]	242^{+10}_{-3}	241^{+5}_{-17}
$V_{\phi,\odot} - V_c$ [km s ⁻¹]	$23.9^{+5.1}_{-0.5}$	$23.1^{+3.6}_{-0.5}$
$\mu_{\text{Sgr A}^*}$ [mas yr ⁻¹]	$6.32^{+0.07}_{-0.70}$	$6.36^{+0.09}_{-0.86}$
$\sigma_R(R_0)$ [km s ⁻¹]	$31.4^{+0.1}_{-3.2}$	$32.2^{+0.2}_{-2.6}$
R_0/h_σ	$0.03^{+0.01}_{-0.27}$	$0.06^{+0.01}_{-0.17}$
$X^2 \equiv \sigma_\phi^2/\sigma_R^2$	$0.70^{+0.30}_{-0.01}$	$0.64^{+0.18}_{-0.02}$

NOTE. — Maximum-likelihood best-fit results; uncertainties are given as 68% intervals of the marginalized PDF for each parameter. The first block of parameters are the basic Galactic parameters: circular velocity $V_c(R_0)$ at the Sun’s location, the derivative of the circular-velocity curve with R , and various other representations of these two basic parameters: the Oort parameters A and B , the rotational frequency Ω_0 at the Sun’s location, and the combination $(B^2 - A^2)/(2\pi G)$ that is relevant in the determination of the local dark matter density using the cylindrical Poisson equation. The second block of parameters describe the Sun’s phase-space position in the Galaxy: distance R_0 to the Galactic center, the Sun’s radial velocity $V_{R,\odot}$ (away from the Galactic center), the Sun’s Galactocentric rotational velocity $V_{\phi,\odot}$, and the Sun’s peculiar velocity with respect to local Galactic rotation $V_{\phi,\odot} - V_c$. We also give the proper motion of Sgr A* derived from the previous parameters assuming that Sgr A* is at rest with respect to the disk. The final block of parameters describe the tracer population sampled by APOGEE: radial velocity dispersion $\sigma_R(R_0)$ at R_0 , the radial scale length h_σ of the radial velocity dispersion (given as R_0/h_σ), and the ratio of the tangential to the radial velocity variance σ_ϕ^2/σ_R^2 .

ear fit). In TABLE 2, we also give the Oort constants A and B corresponding to the V_c and dV_c/dR inferred directly for our sample (for the case of a flat rotation curve, A and B are equal in magnitude and opposite in sign, by definition). We also present the combination $(B^2 - A^2)/(2\pi G)$, which is the correction term that must be added to the local dark-matter density to account for a non-flat rotation curve, when the local dark-matter density is inferred from local vertical kinematics using the cylindrical Poisson equation (e.g., Bovy & Tremaine 2012). It is clear that we constrain this correction term to be smaller than a fraction of the local dark-matter density: $-0.0025 M_\odot \text{ pc}^{-3} < (B^2 - A^2)/(2\pi G) < 0.0004 M_\odot \text{ pc}^{-3}$, compared to a local dark-matter density of $0.008 \pm 0.003 M_\odot \text{ pc}^{-3}$ (Bovy & Tremaine 2012). Thus, the correction for the non-flatness of the rotation curve for our best-fit parameters is approximately zero, and at 68% confidence it lies between -0.1 GeV cm^{-3} and 0.0 GeV cm^{-3} . We also give the rotational frequency Ω_0 at the Sun’s location.

Using a power-law rotation-curve model, we estimate the uncertainty in the rotation curve by evaluating the range of $V_c(R)$ at each R for 10,000 samples from the PDF shown in FIG. 5. Thus, every sample has a power-law rotation curve, but the range at each R does not have to follow a power law itself. This exercise shows whether, *in the power-law model*, the value of $V_c(R)$ is well-

constrained or not for each R ; The result is shown in the left panel of FIG. 6. The same is shown in the right panel of that figure for a fit assuming a cubic-polynomial model for the rotation curve. However, in the latter model we have imposed a prior that $R_0 < 9$ kpc, as a large number of samples from the PDF have $R_0 > 9$ kpc, which we assume to be implausible from prior data (e.g., Ghez et al. 2008; Gillessen et al. 2009). We emphasize that we do not include such a prior in any other part of the analysis presented here. We see that the rotation curve is best constrained at small radii ($4 \text{ kpc} < R < 8 \text{ kpc}$), and that it is largely consistent with being close to flat over the full range of Galactocentric radii considered here.

We also determine the full planar phase-space position of the Sun in the Galactocentric reference frame. The current APOGEE data are relatively insensitive to the value of R_0 . The 68% interval for R_0 for both the flat-rotation-curve and power-law fits is about $8 \text{ kpc} < R_0 < 9 \text{ kpc}$, which is similar to that found for the mock data in Appendix B. The best-fit value is at the lower end of this range: 8.1 kpc when assuming a flat rotation curve, 8 kpc for the power-law rotation-curve fit. The fully marginalized PDF for R_0 in the top, left panel of FIG. 5 is almost entirely flat between $8.0 \text{ kpc} < R_0 < 9.3 \text{ kpc}$.

The Galactocentric motion of the Sun is approximately $V_{R,\odot} = -10.5 \pm 1.0 \text{ km s}^{-1}$, and $V_{\phi,\odot} = 242^{+10}_{-3} \text{ km s}^{-1}$ (in the case of a flat rotation curve) or

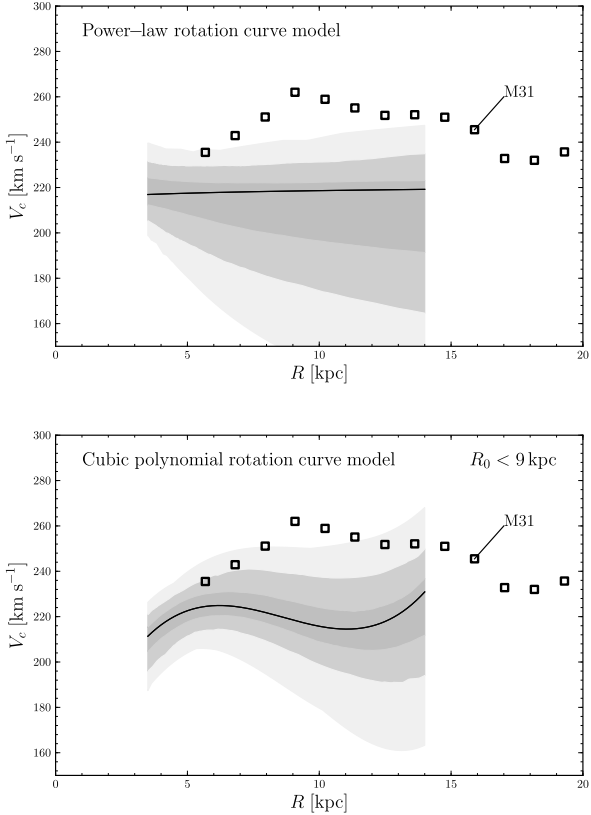


FIG. 6.— The Milky Way’s rotation curve in the range $4 < R < 14$ kpc as inferred from our data for different forms of the shape of the rotation curve. At each R , the range in $V_c(R)$ from 10,000 samples of the PDF—assuming a power-law or cubic-polynomial model for the shape of the rotation curve—is determined and the 68%, 95%, and 99% intervals are shown in varying shades of gray. For the cubic-polynomial model, we impose a prior that $R_0 < 9$ kpc (see text). For comparison, the squares show the rotation curve of M31 from the compilation of Carignan et al. (2006).

$V_{\phi,\odot} = 242^{+5}_{-17}$ km s $^{-1}$ (for a power-law fit to the rotation curve). In the latter fit, there is a strong correlation between V_c and $V_{\phi,\odot}$; the difference between the two is much better constrained: $V_{\phi,\odot} - V_c = 23.1^{+3.6}_{-0.5}$ km s $^{-1}$. The marginalized PDF for $V_{\phi,\odot} - V_c$ in FIG. 5 is well-described by $V_{\phi,\odot} - V_c = 26 \pm 3$ km s $^{-1}$. We discuss the consequences of this solar motion in detail in § 5.3, but we note here that the estimate of the angular motion of the Galactic center that we obtain from combining our fits for $V_{\phi,\odot}$ and R_0 is consistent with the proper motion of Sgr A* as measured by Reid & Brunthaler (2004): our estimate is $\mu_{\text{Sgr A}*} = 6.3^{+0.1}_{-0.7}$ mas yr $^{-1}$, compared to the direct measurement of 6.379 ± 0.024 mas yr $^{-1}$. We discuss the apparent discrepancy between our agreement with the proper motion of Sgr A* and our low value for V_c in § 5.3.

The final block of parameters in TABLE 2 describe the tracer population. The velocity dispersion that we infer for the tracer stars is close to that expected for an old disk population: $\sigma_R(R_0) \approx 32.0^{+0.5}_{-3}$ km s $^{-1}$ for the flat-rotation-curve and power-law fits. The ratio of the tangential-to-radial velocity dispersions squared is $0.69 < X^2 < 1.0$, with the best-fit value at the lower end

of this range. This value is higher than expected from the epicycle approximation for a flat or falling rotation curve, which is $X^2 \leq 0.5$. However, this expectation holds only for a cold disk, and corrections due to the temperature of the old disk population always increase X^2 near R_0 (Kuijken & Tremaine 1991): the Dehnen disk distribution functions of Equation (6) have X^2 that varies spatially, and reaches approximately 0.65 near R_0 (Dehnen 1999). The best-fit value for R_0/h_σ is approximately zero, with non-zero positive values ruled out by the data: the 68% interval is $-0.24 < R_0/h_\sigma < 0.03$. Thus, the radial-velocity dispersion does not drop exponentially with radius with a scale length between $2R_0/3$ and R_0 ; such a drop would be expected from previous measurements of the radial dispersion as a function of R (Lewis & Freeman 1989), or from the observed exponential decline of the vertical velocity dispersion (Bovy et al. 2012b) combined with the assumption of constant σ_z/σ_R . We have attempted fits with two populations of stars with different radial scale lengths (3 kpc and 5 or 6 kpc) and radial-velocity dispersions, but the same radial-dispersion scale length. The best-fit R_0/h_σ remains zero, such that it does not seem that we are seeing a mix of multiple populations that conspire to form a flat σ_R profile.

Even with the best-fit flat radial-dispersion profile, the disk is stable over most of the range in R considered here. The Toomre Q parameter— $Q = \sigma_R \kappa / (3.36 G \Sigma)$ (Toomre 1964)—for a flat rotation curve is

$$Q = 1.72 \left(\frac{\sigma_R}{32 \text{ km s}^{-1}} \right) \left(\frac{V_c}{220 \text{ km s}^{-1}} \right) \left(\frac{R}{8 \text{ kpc}} \right)^{-1} \left(\frac{\Sigma}{50 M_\odot \text{ pc}^{-2}} \right)^{-1}. \quad (9)$$

This expression has $Q > 1$ down to 4.9 kpc and $Q = 0.91$ at $R = 4$ kpc for a constant $\sigma_R(R)$ and a surface density $\Sigma \propto e^{-R/(3 \text{ kpc})}$. Although the disk is marginally unstable in our best-fit model, this conclusion depends strongly on the assumed radial scale length: for $h_R = 3.25$ kpc, $Q > 1$ everywhere at $R > 4$ kpc. The flatness of the inferred σ_R profile also depends on the assumed constancy of X^2 . Actual equilibrium axisymmetric disks, such as those having a Dehnen distribution function (Equation (6)), have a radially-dependent X^2 , with X^2 at $R = 4$ kpc typically smaller than at $R = 8$ to 16 kpc (Dehnen 1999, Figure 4). At $R = 4$ kpc, which for the present data sample is only reached for the $l = 30^\circ$ line of sight, the line-of-sight velocity is entirely composed of the tangential-velocity component, such that any decrease in X^2 leads to an *increase* in σ_R to sustain the same σ_ϕ . Therefore, the true $\sigma_R(R)$ profile presumably *is* falling with R , and the entire disk at $R > 4$ kpc should be stable in our model.

Full PDFs for all of the parameters of the basic models discussed in this section are given in FIG. 5. It is clear that with the exception of V_c and the derivative of the rotation curve— β in the power-law model and dV_c/dR in the linear model—there are no strong degeneracies among the parameters. Also included in this figure are the results from fitting all but one of the 14 APOGEE field for each field: these leave-one-out results show that no single field drives the analysis for any of the parame-

ters.

We compare the best-fit flat-rotation curve model with the data in FIG.s 7 and 8. FIG. 7 shows the raw heliocentric velocities versus Galactic longitude for all of the stars in the sample, as well as the mean for each field, and the prediction for the mean from the best-fit model. This “model mean” is computed by constructing the predicted line-of-sight velocity distribution using Equation (2) and then calculating its mean. The full predicted line-of-sight velocity distribution for each field is shown in FIG. 8 as the smooth curve, which is to be compared with the histogrammed data points for each field. It is clear from FIG. 8 that the fits capture the overall smooth features of the distribution of line-of-sight velocities in each field, including any asymmetry in the distribution. However, it is also obvious that some of the model predictions are shifted from the observed histograms. This effect also appears in the comparison between the data mean and model mean for each field in the lower panel of FIG. 7. There appears to be a distinct pattern in these residuals. Thus, *the best-fit axisymmetric model fails to account for $\approx 10 \text{ km s}^{-1}$ smooth deviations in the velocity field*. These deviations are likely due to non-axisymmetric streaming motions, which are expected at this level of accuracy; We discuss this further in § 5.3. With the exception of the $l = 60^\circ$ field, the data seem to follow the smooth velocity distribution quite well, albeit somewhat shifted on average.

4.2. Systematics

The basic models presented in the previous section are potentially subject to systematic uncertainties, which we discuss in this section. These uncertainties are mainly related to the distances of the stars in our sample, as these are obtained from somewhat uncertain models of the color–magnitude distribution of giant stars in the near-infrared J , H , and K_s bands. We discuss here the influence of our assumed value for the scale length of the stars, of potential systematic offsets in the preliminary APOGEE metallicities used to inform the photometric distances, of systematic distance uncertainties, and of the impact of mis-estimated interstellar extinction and absorption. We also discuss the effect of binary contamination, of using a different set of stellar isochrones for distance estimation, and of modeling the data using many underlying populations of stars, with velocity dispersions smoothly varying with age.

In our fits, we have simply assumed a value of 3 kpc for the radial scale length, h_R , of the sample of stars used in the analysis. This assumption is based on the fact that, locally, the dominant solar-metallicity disk population has this scale length (Bovy et al. 2012c). The parameter h_R enters our analysis in two ways, the first being in the asymmetric-drift correction (Equation (5)), and the second being in the prior on the distance distribution (Equation (A1)). The former of these is the most important for determining $V_c(R)$. Changing h_R to 2 kpc—which is highly unlikely, given that such a short scale length is not observed for any of the metal-rich, “thin disk” populations in the solar neighborhood (Bovy et al. 2012c)—increases the best-fit value to $V_c = 223 \text{ km s}^{-1}$ for a model with a flat rotation curve, and to $V_c = 220 \text{ km s}^{-1}$ for a power-law rotation curve. Increasing h_R to 4 kpc

decreases the best-fit value to $V_c(R_0) = 217 \text{ km s}^{-1}$. Similar changes happen for the mock data sets described in Appendix B. Therefore, we conclude that the assumed radial scale length has a negligible influence on the inferred V_c .

To determine the influence of systematic offsets in the metallicities used in the photometric distances, we have performed fits allowing for a single metallicity offset, $\Delta[\text{Fe}/\text{H}]$, for all of the stars in the sample, for a model with a flat rotation curve. We find that the best-fit $\Delta[\text{Fe}/\text{H}] = -0.15 \pm 0.02 \text{ dex}$, but the best-fit value of V_c is unchanged, as is its uncertainty (see FIG. 5 for the $\Delta[\text{Fe}/\text{H}]$ – V_c PDF). Although an offset of -0.15 dex might seem large, this offset should not be thought of as a measurement of $[\text{Fe}/\text{H}]$ for the stars in our sample, because the photometric-distance PDFs, such as that in FIG. 11, are relatively insensitive to large changes in $[\text{Fe}/\text{H}]$, especially at the high-metallicity end. We have also performed a fit with a different $\Delta[\text{Fe}/\text{H}]$ for inner ($l \leq 90^\circ$) and outer-disk fields. Such a fit finds $\Delta[\text{Fe}/\text{H}] = -0.12 \pm 0.03 \text{ dex}$ for the outer-disk fields, and $\Delta[\text{Fe}/\text{H}] = 0.70 \pm 0.06 \text{ dex}$ for the inner-disk fields, with a best-fit $V_c = 220 \text{ km s}^{-1}$; see FIG. 5 for the full PDF of the $\Delta[\text{Fe}/\text{H}]$ and V_c . As discussed previously, the photometric-distance PDFs are largely insensitive to changes in $[\text{Fe}/\text{H}]$ at high $[\text{Fe}/\text{H}]$; the Padova isochrones also have an upper limit of $[\text{Fe}/\text{H}]_{\text{max}} = 0.45 \text{ dex}$, such that increasing a star’s $[\text{Fe}/\text{H}]$ beyond this has no effect, because we then use $[\text{Fe}/\text{H}]_{\text{max}}$. Therefore, even a change of $\Delta[\text{Fe}/\text{H}] = 0.7 \text{ dex}$ has a negligible influence on the inner, high-metallicity, disk fields. In none of these fits is our inferred range for R_0 affected.

Similarly, we have performed fits allowing for a single distance-modulus offset, $\Delta\mu$, to be applied to all of the stars in our sample, or for a separate offset for inner- and outer-disk fields. In the former case, we find $\Delta\mu = -0.27 \pm 0.06$, corresponding to a $12 \pm 3\%$ distance offset, without any influence on the inferred value of V_c . In the inner/outer offset fit, we find 23% smaller distances at $l \leq 90^\circ$, and 20% larger distances in the outer disk, again with a negligible influence on the best-fit V_c ($V_c = 221 \text{ km s}^{-1}$), but with a second minimum around $V_c = 190 \text{ km s}^{-1}$, and a wider V_c PDF that is, however, at $V_c < 235 \text{ km s}^{-1}$ at 99% confidence. A more physical effect is to allow for an offset in the extinction, ΔA_H , again using a single offset for the whole sample, or splitting the sample into inner- and outer-disk fields. A single extinction offset is well-constrained to be small: $\Delta A_H = -0.01 \pm 0.01$. Similarly, the best-fit extinction offset in the outer disk is $\Delta A_H = 0 \pm 0.02$, while in the inner disk we find some evidence for mis-estimated extinction, with $\Delta A_H = -0.2 \pm 0.03$. In both of these cases, the best-fit V_c increases by 1 km s^{-1} or less, and the uncertainties remain approximately the same (see FIG. 5).

As discussed in § 2, we do not limit the sample to stars for which multiple velocity epochs are available that indicate that they are not part of a multiple system. Such a cut significantly reduces the longitudinal coverage of our sample. When we do apply this cut, we find that the best fits for V_c and all other parameters are unchanged from the results for our basic flat-rotation-curve model in § 4.1, albeit with larger uncertainties. We find in particular that $V_c = 217 \pm 7 \text{ km s}^{-1}$, but the uncertainties in

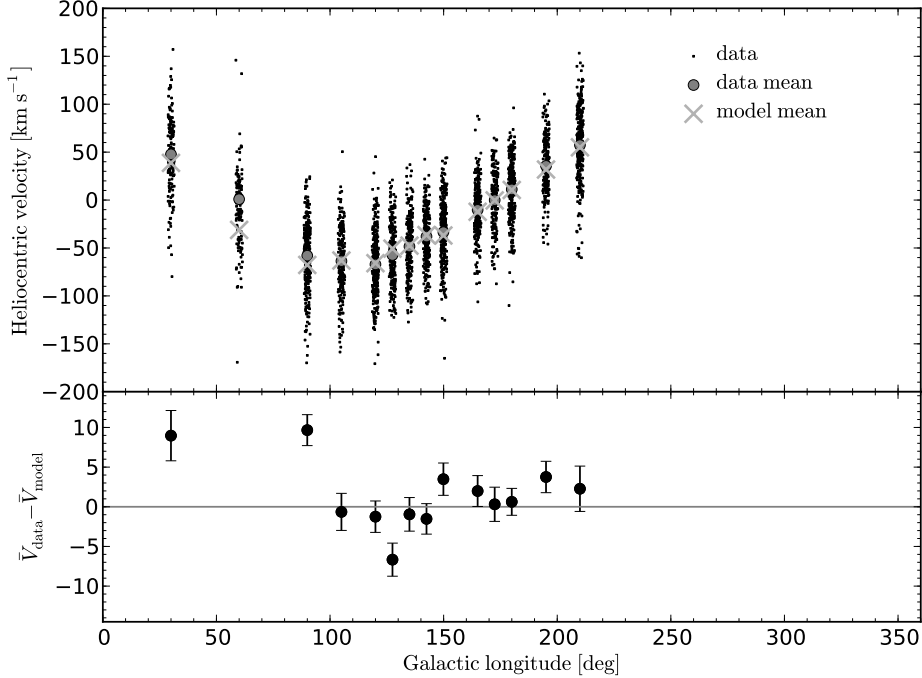


FIG. 7.— Comparison between our best-fit flat-rotation-curve model and the data. The top panel shows the individual heliocentric velocities of stars in our sample as a function of Galactic longitude, with the mean for each APOGEE field indicated by a gray dot. The prediction for this mean from the best-fit model is shown as the gray cross. The bottom panel shows the difference between the data mean \bar{V}_{data} and the model mean \bar{V}_{model} . Note that the residual for the $l = 60^\circ$ field in the bottom panel is missing as it is larger than 15 km s^{-1} .

the position and velocity of the Sun are much increased.

In Appendix A, we describe how we employ Padova isochrones to estimate photometric distances to the stars in our sample. When instead we use isochrones from the BaSTI library (Pietrinferni et al. 2004), using the filter transformation from Carpenter (2001) to transform K_s to the K -band filter used by BaSTI, we find that the results of our basic models (both with a flat and a power-law rotation curve) are essentially unchanged (with changes in V_c of about 1 km s^{-1}).

To determine whether our results change when we fit the data as a mix of multiple stellar populations, with velocity dispersions varying from that of a young population to that of the oldest disk population, we have performed a fit where the likelihood for V_{los} in Equation (1) is generalized to

$$\begin{aligned} p(V_{\text{los}}|l, b, (J - K_s)_0, H_0, [\text{Fe}/\text{H}], V_c(R), R_0, V_{R,\odot}, V_{\phi,\odot}, \text{iso}) \\ = \sum_i P(i) p(V_{\text{los}}|l, b, (J - K_s)_0, H_0, [\text{Fe}/\text{H}], V_c(R), R_0, \\ V_{R,\odot}, V_{\phi,\odot}, \text{DF}_i, \text{iso}), \end{aligned} \quad (10)$$

where DF_i is the single-Gaussian population model used before, with dispersion at age τ_i

$$\sigma_{R,i} = \sigma_{R,0} \left(\frac{\tau_i + 0.1 \text{ Gyr}}{10.1 \text{ Gyr}} \right)^{0.38} \quad (11)$$

and using an exponentially-declining star-formation history, such that $P(i) \propto e^{\tau_i/(8 \text{ Gyr})}$. This model follows

the fit of Aumer & Binney (2009) in the solar neighborhood. We use a mix of 20 equally age-spaced populations between 1 and 10 Gyr, and find $V_c = 216 \pm 7 \text{ km s}^{-1}$, showing that this alternative model does not change our results; the full $V_c - R_0$ PDF is shown in FIG. 5. This model has $\sigma_{R,0} = 38 \pm 2 \text{ km s}^{-1}$, as expected for the old, “thin disk” population.

5. DISCUSSION

5.1. Effect of Non-Axisymmetric Features

In the fits in § 4, we have assumed axisymmetric models for the velocity field in the Galactic disk. However, the Milky Way is known to have some non-axisymmetric structures, such as the central bar (Blitz & Spergel 1991; Binney et al. 1991), spiral arms (e.g., Drimmel & Spergel 2001), and a potentially triaxial halo (Law et al. 2009), that may influence the measurement performed in this paper. Because we use a warm disk population as dynamical tracers, we can expect the influence of any non-axisymmetry to be smaller than for the colder gas tracers used in other studies (e.g., Levine et al. 2008), because warm tracers respond less strongly to non-axisymmetric perturbations to the Milky Way potential than cold tracers (Lin et al. 1969).

We have calculated the velocity field for a warm tracer population in various non-axisymmetric models (see J. Bovy, 2013, in preparation, for full details). We follow the procedure of Dehnen (2000) and Bovy (2010) to calculate the velocity distribution at a given position for a given non-axisymmetric model for the disk, by per-

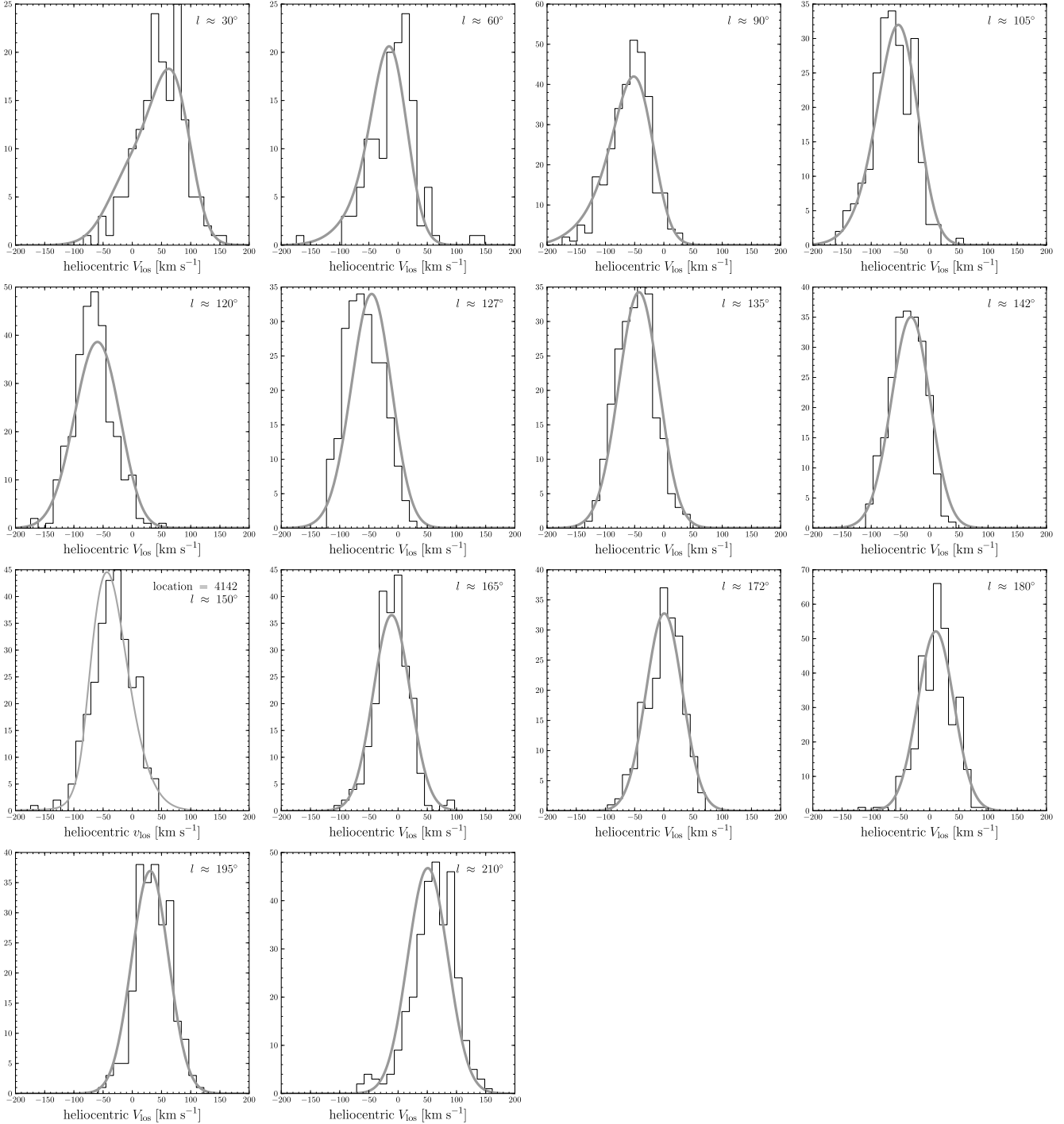


FIG. 8.— Comparison between the full line-of-sight heliocentric velocity distributions of the data and the best-fit flat-rotation-curve model. Fields are ordered by increasing longitude. The agreement between the gray model curve and the data is good, except for some offsets in the mean of the distributions, as is also clear from FIG. 7.

forming backward orbit integrations until before the onset of the non-axisymmetric perturbation in an axisymmetric disk. At that time, the distribution function of the pre-existing axisymmetric disk is evaluated. By the conservation of phase-space density, this probability is equal to the current probability of the phase-space starting point of the orbit integration. We assume a flat rotation curve for the axisymmetric part of the potential, and we model the initial, axisymmetric distribution function

as a Dehnen distribution function (Equation (6)) with a velocity dispersion of $0.2 V_c$, a radial scale length of $R_0/3$ and a dispersion scale length of R_0 . These parameters are close to the best-fit parameters for the APOGEE tracer population.

We calculate the mean velocity field for the bar model of Dehnen (2000), and use it to construct the mean, non-axisymmetric V_{los} field. This field is then applied as part of the model, and the result for the mean line-

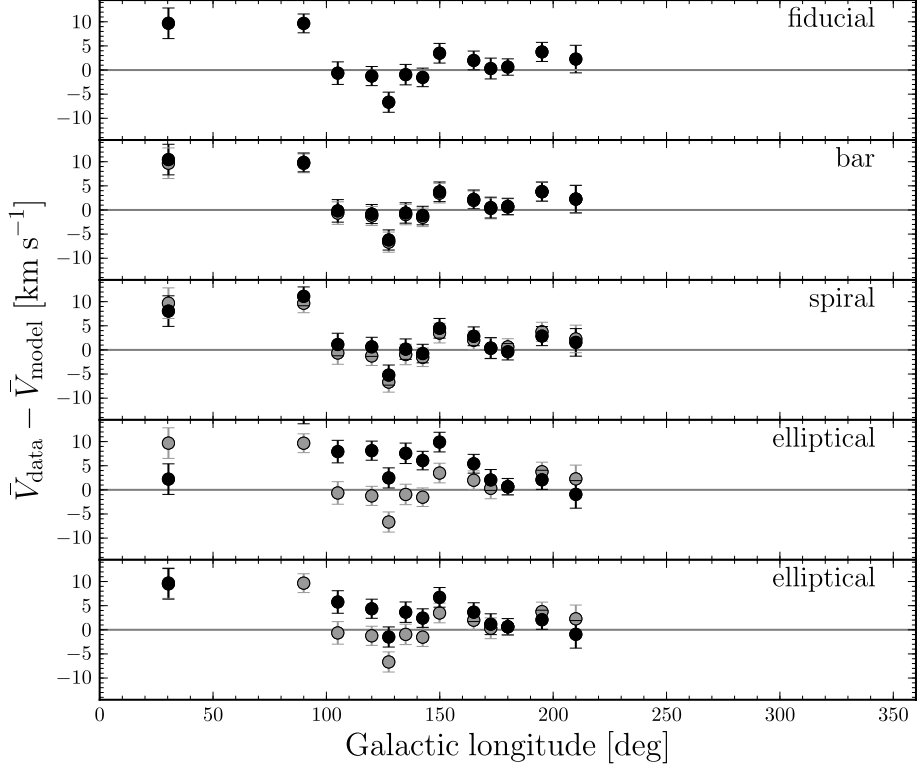


FIG. 9.— Influence of non-axisymmetry on the predicted mean of the V_{los} distributions. The flat-rotation curve model of TABLE 2 and FIG.s 7 and 8 is displayed in the uppermost panel. Non-axisymmetric models shown are: the model for the Milky Way bar of Dehnen (2000); a two-armed logarithmic spiral with a fractional amplitude of 1% and a pitch angle of -15° ; elliptical disk models of Kuijken & Tremaine (1994) with an amplitude of 5% and position angles of 0° (fourth panel) and -45° (bottom panel). All models are calculated for a warm disk population with $\sigma_R(R_0) = 44 \text{ km s}^{-1}$ and are adiabatically grown in an initially equilibrium, axisymmetric disk. While the influence of bar and spiral structure perturbations is small, an elliptical disk model can reduce the size of the residuals. This figure only shows the influence of non-axisymmetry on the mean of the line-of-sight velocities in each field; much more information is of course contained in the full distribution of line-of-sight velocities.

of-sight velocity in each field is shown in FIG. 9—there is of course much more discretionary power in the full distribution functions. In the same manner, we calculate the mean V_{los} field for a two-armed logarithmic spiral with a fractional potential-amplitude of 1% of the background, axisymmetric potential, a pitch angle of -15° , an angular frequency of $0.65 \Omega_0$ (placing the Sun near the 4:1 inner Lindblad resonance), and an angle between the Sun–Galactic-center line and the line connecting the peak of the spiral pattern at the solar radius of 20° . We do the same for models with a flat elliptical (stationary, $m = 2$) distortion to the potential (see Kuijken & Tremaine 1994), with a fractional amplitude of 5% and position angles of 0° and -45° with respect the the Sun–Galactic center line. All of these perturbations were adiabatically grown. We see in FIG. 9 that the influence of the bar and spiral structure is negligible in the mean V_{los} velocity field. An elliptical, $m = 2$, perturbation could distort the mean velocity field in a way that would affect our analysis. Naively, the model in the bottom panel of FIG. 9 significantly reduces the residuals between the best-fit \bar{V}_{los} and the data \bar{V}_{los} .

It is clear that the data used in this paper could be

used to constrain non-axisymmetric perturbations to the axisymmetric potential assumed here. We defer a full treatment of this to a subsequent paper.

5.2. Comparison with Other Determinations of the Local Circular Velocity

There have been many previous determinations of the local circular velocity, and we discuss here how our new measurement compares to these. Determinations of the local circular velocity can be roughly divided into two groups: measurements of the Sun’s velocity with respect to an object or population assumed to be at rest with respect to the Galactic center (e.g., Sgr A* or a population of halo objects), or direct measurements of the local radial force (e.g., by determining the Oort constants or the orbit of a stream of stars). The former directly measure the Sun’s Galactocentric velocity, $V_{\phi,\odot}$, but must assume a value for the Sun’s motion with respect to the circular orbit at R_0 to arrive at $V_c(R_0)$. The most direct measurement of this kind is the combination of the precisely measured proper motion of Sgr A* (Reid & Brunthaler 2004) with the distance to the Galactic center determined from the Keplerian orbits of S stars in the innermost parsec (Ghez et al. 2008; Gillessen et al. 2009).

These measurements give $R_0 \approx 8$ kpc, which combined with the proper motion of Sgr A* of $30.24 \text{ km s}^{-1} \text{ kpc}^{-1}$, yields a total solar velocity of 242 km s^{-1} . As noted before, this result is entirely consistent with our inferred value of the angular motion of the Galactic center, and with our $V_{\phi,\odot} = 242^{+10}_{-3} \text{ km s}^{-1}$. The discrepancy between the value of $V_c = 229 \text{ km s}^{-1}$ in Ghez et al. (2008) (or higher measurements also based on the proper motion of Sgr A*) and our $V_c = 218 \text{ km s}^{-1}$ is therefore *entirely due to our different value for the solar velocity with respect to V_c* , and intrinsically these measurements are consistent. Similarly, the recent measurements of $V_{\phi,\odot} = 276 \pm 23 \text{ km s}^{-1}$ and $V_{\phi,\odot} = 244 \pm 14 \text{ km s}^{-1}$ using the kinematics of the Sgr stream (Carlin et al. 2012) are consistent with our measurement of the solar velocity.

Measurements based on the Oort constants (e.g., Feast & Whitelock 1997), or the dynamics of a cold stellar stream (Koposov et al. 2010), also indicate that $V_c \sim 220 \text{ km s}^{-1}$. The measurement of the Oort constants from *Hipparcos* proper motions by Feast & Whitelock (1997) directly measure the angular frequency of the local circular orbit, independent (in principle) from the solar motion: $\Omega_0 = V_c/R_0 = 27.2 \pm 0.9 \text{ km s}^{-1} \text{ kpc}^{-1}$. This value is consistent with our determination (see TABLE 2) $\Omega_0 = 27.0^{+0.3}_{-3.5} \text{ km s}^{-1} \text{ kpc}^{-1}$. The determination of $V_c = 221 \pm 18 \text{ km s}^{-1}$ of Koposov et al. (2010) from fitting an orbit to the cold GD-1 stellar stream at $R \sim 10$ kpc is clearly consistent with our measurement, although note that they assumed the $V_{\phi,\odot} - V_c = 5.25 \text{ km s}^{-1}$ value for the solar motion from Dehnen & Binney (1998).

The recent measurement of $V_c = 254 \pm 16 \text{ km s}^{-1}$, from the kinematics of masers in the Galactic disk (Reid et al. 2009), was shown to have an overly optimistic precision by Bovy et al. (2009a), who concluded from a more general model for the distribution function of the masers that these data only imply $V_c = 246 \pm 30 \text{ km s}^{-1}$. The measurement of V_c from the maser kinematics also assumes that $V_{\phi,\odot}$ is given by V_c plus the locally-determined solar motion of $\sim 10 \text{ km s}^{-1}$. Apart from indicating a high value for V_c , albeit with a large uncertainty, the masers were also found to be lagging with respect to circular motion by about 15 km s^{-1} , a large offset for a young and relatively cold tracer population. This offset cannot be explained by the asymmetric drift and it is physically implausible since it requires the masers to have more eccentric orbits than most of the young stars (McMillan & Binney 2010). Requiring the masers to be on circular orbits assuming a flat rotation curve leads to a solar motion of $V_{\phi,\odot} - V_c = 18.6 \pm 2.4 \text{ km s}^{-1}$ and $V_c = 232 \pm 24$ (McMillan & Binney 2010), in good agreement with our measurements. Our measurement, however, relies on the theoretically well-motivated asymmetric-drift correction that is a direct consequence of the collisionless Boltzmann equation.

Therefore, we conclude that our measurement of V_c is consistent with previously reported values. Compared to other determinations, our measurement of V_c is one of the most highly precise, and unlike many other measurements, it does not require assumptions about the relation between the solar motion and V_c .

Our data *strongly* rule out that the Milky Way's

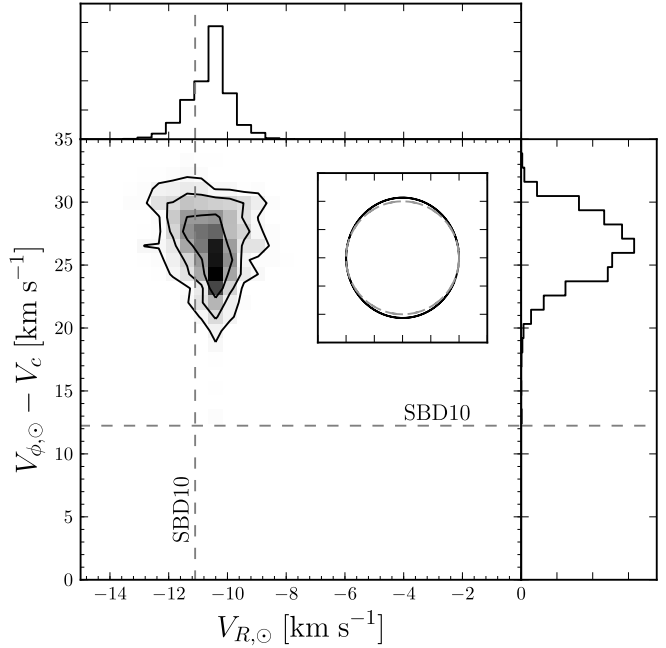


FIG. 10.—Sun's peculiar velocity with respect to circular motion. This figure shows the posterior probability distribution function of the Sun's velocity with respect to the circular orbit at the solar radius. The measurement of the Sun's motion with respect to the orbit of a zero velocity dispersion population from Schönrich et al. (2010; SBD10) is indicated by dashed lines. The fact that our measurement of the Sun's rotational peculiar velocity does not agree with the SBD10 value may indicate that the closed orbit at the solar radius is not circular, due to non-axisymmetry at the level of 10 km s^{-1} . The inset shows this non-circular closed orbit (spatially to scale) if the non-axisymmetry is due to ellipticity of the disk (e.g., Kuijken & Tremaine 1994); the dashed gray curve is the circular orbit. Alternatively, the locally-determined solar motion may be off by $\sim 10 \text{ km s}^{-1}$.

circular velocity at the solar radius is $> 235 \text{ km s}^{-1}$. Marginalizing over all of the systematics discussed in § 4.2, $V_c < 235 \text{ km s}^{-1}$ at $> 99\%$ confidence. Fixing V_c to 250 km s^{-1} with $R_0 = 8$ kpc or 8.4 kpc leads to a best-fit with much larger χ^2 : $\Delta\chi^2 = 47$ ($\sim 5\sigma$) and $\Delta\chi^2 = 34$ ($\sim 3.7\sigma$), respectively.

Our measurement that the Milky Way's rotation curve is essentially flat over $4 \text{ kpc} < R < 14 \text{ kpc}$ agrees with measurements based on the kinematics of HI emission (e.g., Gunn et al. 1979; Merrifield 1992) and with the local measurement of the Oort constants (Feast & Whitelock 1997).

5.3. Implications for the Motion of the LSR

We found in § 4, in both the flat- and power-law-rotation-curve models, that the Sun's velocity with respect to the center of the Galaxy—a distinct parameter from V_c in our fit—is larger than $V_c(R_0)$ by $\sim 24 \text{ km s}^{-1}$. Defining the Rotational Standard of Rest (RSR; Shuter 1982) as the circular velocity in the axisymmetric approximation to the full potential, this solar motion with respect to the RSR is much larger than that measured by applying Strömgren's asymmetric-drift relation to local samples of stars. The asymmetric-drift relation is used to estimate the velocity of the zero-dispersion orbit by extrapolating the relation given in

Equation (5) from warmer samples of stars to $\sigma_R = 0$; it is this zero-dispersion orbit that is typically what is meant by the LSR (Fich & Tremaine 1991). Such analyses of the *Hipparcos* data yield a solar motion with respect to the LSR that is somewhere between 5 and 13 km s⁻¹ (Dehnen & Binney 1998; Hogg et al. 2005; Schönrich et al. 2010); 13 km s⁻¹ is also the offset of the average rotational velocity of nearby stars (e.g., Allende Prieto et al. 2004). The discrepancy between our determination of the solar velocity with respect to the RSR, and that with respect to the LSR, is clearly shown in FIG. 10, where the PDF for $V_{\phi,\odot} - V_c, V_{R,\odot}$ is shown for the flat-rotation curve model, together with the locally-measured motion with respect to the LSR of Schönrich et al. (2010). The analogous figure for the power-law rotation-curve fit has an essentially identical appearance. It is clear that the locally-measured solar motion $V_{\phi,\odot}$ is not equal to our globally-measured solar motion to very high significance. Or, equivalently, the motion of the RSR is not the same as that of the LSR: the LSR seems to rotate ~ 12 km s⁻¹ faster than the RSR.

This discrepancy may result from a breakdown in the assumptions of the locally-measured solar motion using Strömgren's asymmetric-drift relation. As convincingly shown by Schönrich et al. (2010), the neglect of the radial metallicity gradient in the analysis of Dehnen & Binney (1998) leads to a correction of ~ 7 km s⁻¹, but further improvements in the chemical-evolution model of Schönrich et al. (2010) might lead to further corrections. The local velocity distribution has also long been known to contain various streams or “moving groups” (e.g., Kapteyn 1905; Schwarzschild 1907; Eggen 1986; Dehnen 1998; Bovy et al. 2009b) that are likely of a dynamical origin (Bensby et al. 2007; Famaey et al. 2008; Bovy & Hogg 2010; Sellwood 2010) and contain a significant fraction of the nearby stars (Bovy et al. 2009b). These moving groups make an accurate determination of the solar motion challenging. As such, the locally-determined correction for the Sun’s motion with respect to the LSR may well be incorrect by ~ 5 km s⁻¹ or more. A solar motion of ~ 24 km s⁻¹ rather than ~ 12 km s⁻¹ is not much more unlikely given the distribution function for a ~ 5 Gyr population: using a Dehnen distribution function (Equation (6)) with a radial dispersion of 30 km s⁻¹ (Equation (11)) and assuming our best-fit model gives $P(V_{\phi,\odot} - V_c > 12 \text{ km s}^{-1}) \approx 0.2$ and $P(V_{\phi,\odot} - V_c > 24 \text{ km s}^{-1}) \approx 0.1$.

However, if Strömgren's relation leads to a solar motion with respect to the LSR that is different from the globally-determined solar motion with respect to the RSR, the most straight-forward interpretation is that LSR’s orbit is not circular, but deviates from circularity by about 10 km s⁻¹ because of large-scale, non-axisymmetric streaming motions. The deviation cannot be much larger than this value, as the *radial* component of the solar motion as determined from local samples agrees with our global measurement. As our measurement of the circular velocity is mainly at azimuths $\phi \lesssim 45^\circ$, this 10 km s⁻¹ deviation must happen over this angular scale.

There is mounting evidence for the existence of stream-

ing motions in the Galactic disk of this magnitude. There has been a long-standing discrepancy of ~ 7 km s⁻¹ between the rotation curves determined from first ($l < 90^\circ$) and fourth ($l > 270^\circ$) quadrant tangent-point measurements (e.g., Kerr 1962; Gunn et al. 1979; Levine et al. 2008), which could indicate streaming motions. Similarly, the analysis of the extreme line-of-sight velocity of HI emission toward $l \sim 90^\circ$ leads to differences in V_c of approximately 30 km s⁻¹, albeit with large uncertainties (Knapp et al. 1979; Jackson & Kerr 1981; Jackson 1985). The fact that the maximum line-of-sight velocity in both CO and 21-cm data reaches zero at $l \sim 70^\circ$, rather than at $l = 90^\circ$, has been used to argue that the LSR moves ahead of V_c with a speed of ~ 7.5 km s⁻¹ (Shuter 1982; Clemens 1985), similar to the offset we find. More recently, an analysis of line-of-sight velocities from the RAVE has found a gradient, $d\bar{V}_R/dR$, in the mean radial velocity, \bar{V}_R , of ~ 3 km s⁻¹ kpc⁻¹, and large streaming motions in both \bar{V}_R and the mean tangential velocity, \bar{V}_ϕ , within a few kpc from the Sun (Siebert et al. 2011).

As a simple exploration of this possibility, we have computed the closed orbit at R_0 in a model for the Milky Way disk where this streaming motion is due to ellipticity of the disk, following Kuijken & Tremaine (1994). We use a flat rotation curve, with a $\cos(2\phi)$ perturbation of constant ellipticity having an amplitude of 14 km s⁻¹. Such a perturbation could arise if, for example, the halo is triaxial (e.g., Law et al. 2009). The closed orbit is shown to scale in the inset in FIG. 10; it has an eccentricity of 0.06.

Regardless of the origin of the discrepancy between our globally-measured solar motion and the locally-measured value, our larger preferred value of $V_{\phi,\odot} - V_c$ means that the Sun is likely closer to the pericenter of its orbit around the Galactic center than previously believed. Revising $V_{\phi,\odot} - V_c$ upward by 12 km s⁻¹ increases the eccentricity of the Sun’s orbit to ~ 0.1 from ~ 0.06 and increases its mean Galactocentric radius to ~ 8.9 kpc from ~ 8.5 kpc. Such a large mean radius increases the tension between the Sun’s high metallicity compared to local stars (Wielen et al. 1996), although the peak of the local metallicity distribution may be closer to solar metallicity than previously believed (e.g., Casagrande et al. 2011).

Finally, we address what our results imply for dark-matter direct-detection experiments, and for correcting the motion of Galactic and extra-galactic objects for the motion of the Sun. Both of these applications essentially require knowledge of the *total* Galactocentric solar velocity, $V_{\phi,\odot}$, to transform velocities into the Galactocentric (dark-matter-halo) rest frame²⁵. Although this motion is often decomposed as V_c plus the Sun’s motion with respect to V_c , our results in this paper show that this is unnecessarily dangerous, as it requires the *strong assumption* that the LSR is on a circular orbit, such that $V_{\phi,\odot} = V_c + V_{\phi,\odot,LSR}$, where the final term is the solar velocity with respect to the LSR. Our results in § 4 strongly rule out that this assumption holds for the currently accepted solar motion of ~ 12 km s⁻¹.

²⁵ The one exception is that in the Standard Halo Model, the velocity dispersion of the isothermal halo is given by $V_c/\sqrt{2}$. However, the velocity dispersion of the halo is better determined directly from observations than by using this assumption.

However, this approach is entirely unnecessary for correcting velocities to the Galactocentric rest frame, as the proper motion of Sgr A* combined with the “clean” estimate of R_0 from Galactic-center dynamics shows that $V_{\phi,\odot} \approx 242 \text{ km s}^{-1}$, which agrees with our measured value of $V_{\phi,\odot}$. Adopting a standard $V_{\phi,\odot} = 242 \text{ km s}^{-1}$ for correcting velocities for the Sun’s motion, and decoupling this correction from the question of the true value of V_c , would therefore be helpful.

5.4. Implications for the Mass of the Milky Way

We can use our measurement of the inner rotation curve of the Milky Way to estimate the Milky Way’s total dark-halo mass. We combine the measurements in this paper with those of the Milky Way’s outer rotation curve ($R \gtrsim 20 \text{ kpc}$) of Xue et al. (2008) (specifically, taking the measurements using simulation II in Table 3 of that paper). Based on FIG. 6 and TABLE 2, we add our measurement as a flat rotation curve with $V_c = 218 \text{ km s}^{-1}$, evaluated at three radii with uncertainties of 3 km s^{-1} , 6 km s^{-1} , and 10 km s^{-1} at $R = 4 \text{ kpc}$, $R = 8 \text{ kpc}$, and $R = 12 \text{ kpc}$, respectively (removing the measurements at $R = 7.5 \text{ kpc}$ and $R = 12.5 \text{ kpc}$ from Xue et al. 2008). We also use our recent measurements of the local density of dark matter, $\rho_{\text{DM}} = 0.008 \pm 0.003 M_\odot \text{ pc}^{-3}$ (Bovy & Tremaine 2012), and of the disk scale length, $h_R = 3.25 \pm 0.25 \text{ kpc}$ (Bovy et al. 2012b), revising the measurement from the latter paper downward to correct for the influence of the dark halo on that measurement.

We model the Milky Way’s potential as the combination of a bulge component with a Hernquist profile with a scale length of 600 pc, a disk component with a scale height of 300 pc (Bovy et al. 2012a) and a scale length that is a free parameter, and a Navarro-Frenk-White halo (NFW; Navarro et al. 1997), with a scale radius that is a free parameter (i.e., without constraint on the concentration). The relative contributions of these three components are free parameters. We then fit the data given in the previous paragraph, and we find that $M_{\text{halo}} = 8_{-2}^{+8} \times 10^{11} M_\odot$. The total mass of the Milky Way is $\sim 8.5 \times 10^{11} M_\odot$.

This “low” estimate for the mass of the Milky Way likely makes it less massive than M31, which has an estimated dark-halo mass of $14 \times 10^{11} M_\odot$ (Watkins et al. 2010). This measurement leads to a combined mass for the Local Group of $\sim 2.4 \times 10^{12} M_\odot$, which is consistent with the Local-Group-timing-argument within the large cosmic scatter (van der Marel et al. 2012). Our measurement of $V_c = 218 \pm 6 \text{ km s}^{-1}$ combined with its estimated I -band magnitude of -22.3 mag makes the Milky Way underluminous with respect to the Tully-Fisher relation of external spiral galaxies by about 1σ (see Flynn et al. 2006).

6. CONCLUSION

In this paper, we have measured the Milky Way’s rotation curve over the range $4 \text{ kpc} < R < 14 \text{ kpc}$ from the new APOGEE data set of kinematically-warm stellar tracers at large distances from the Sun. Our measurement is not “clean”, in the sense of being a geometric measurement such as that provided by tangent-point observations of HI emission or by a measurement of the

Sun’s motion relative to an object assumed to be at rest with respect to the Galactic center. Because we use a warm stellar population, we must correct for the offset between the average rotational velocity of this population and the circular velocity—the asymmetric drift—using a dynamical Jeans model. However, the fact that our measurement uses a dynamical effect, rather than being purely geometric, has the advantage that we unambiguously measure $V_c(R)$ in the sense of the radial force at R , and that we can measure the solid-body-rotation contribution to the rotation curve, in contrast to HI measurements.

Our main results are discussed in § 4. We find that the Milky Way’s rotation curve is approximately flat over $4 \text{ kpc} < R < 14 \text{ kpc}$, with $V_c(R_0) = 218 \pm 6 \text{ km s}^{-1}$. TABLE 2 summarizes our results, and provides some alternative representations, such as the Oort constants, the local rotational frequency, and the contribution of the non-flatness of the rotation curve to a cylindrical-Poisson-equation determination of the local surface-mass and dark-matter densities. We simultaneously measure the Sun’s velocity in the Galactocentric rest frame—these are independent free parameters in our model—and find that $V_{R,\odot} = -10 \pm 1 \text{ km s}^{-1}$ and the angular motion of the Galactic center $\mu = 6.3_{-0.7}^{+0.1} \text{ mas yr}^{-1}$. These values are consistent with previous studies. Our measurement of $V_{\phi,\odot} = 242_{-3}^{+10} \text{ km s}^{-1}$ then leads to a solar offset from V_c that is larger than the locally-measured value ($\sim 12 \text{ km s}^{-1}$; Schönrich et al. 2010) by $14 \pm 3 \text{ km s}^{-1}$. This result may indicate that the challenging local measurement of the solar motion is incorrect or that the solar velocity is influenced by non-axisymmetric streaming motions that put the LSR on a non-circular orbit.

Looking forward, we expect to accurately measure the atmospheric parameters and abundances other than [Fe/H] from the high-resolution APOGEE spectra in the near future. This will improve the measurements described in this paper by (a) providing better dwarf/giant separation, (b) allowing for more direct and more precise distances to be derived, and (c) letting the analysis be conducted on different chemically-defined populations of stars. In particular, this will allow for a more detailed investigation into the signatures of non-axisymmetric dynamics in our data.

The data upon which the measurements presented in this paper are based will be released as part of SDSS-III’s Data Release 10 in the summer of 2013.

It is a pleasure to thank Scott Tremaine for many illuminating discussions about this work. We also thank Jennifer Johnson, Mark Reid, Hans-Walter Rix, and Greg Stinson for helpful comments. J.B. was supported by NASA through Hubble Fellowship grant HST-HF-51285.01 from the Space Telescope Science Institute, which is operated by the Association of Universities for Research in Astronomy, Incorporated, under NASA contract NAS5-26555. J.B. was partially supported by SFB 881 funded by the German Research Foundation DFG and is grateful to the Max-Planck Institut für Astronomie for its hospitality during part of the period during which this research was performed. T.C.B. acknowledges partial support by grants PHY 02-16783 and PHY

08-22648: Physics Frontiers Center/Joint Institute for Nuclear Astrophysics (JINA), awarded by the U.S. National Science Foundation. This research made use of the *emcee* MCMC sampler (Foreman-Mackey et al. 2012).

This publication makes use of data products from the Two Micron All Sky Survey, which is a joint project of the University of Massachusetts and the Infrared Processing and Analysis Center/California Institute of Technology, funded by the National Aeronautics and Space Administration and the National Science Foundation.

This publication makes use of data products from the Wide-field Infrared Survey Explorer, which is a joint project of the University of California, Los Angeles, and the Jet Propulsion Laboratory/California Institute of Technology, funded by the National Aeronautics and Space Administration.

Funding for SDSS-III has been provided by the Alfred P. Sloan Foundation, the Participating Institutions, the National Science Foundation, and the U.S. Department

of Energy Office of Science. The SDSS-III web site is <http://www.sdss3.org/>.

SDSS-III is managed by the Astrophysical Research Consortium for the Participating Institutions of the SDSS-III Collaboration including the University of Arizona, the Brazilian Participation Group, Brookhaven National Laboratory, University of Cambridge, Carnegie Mellon University, University of Florida, the French Participation Group, the German Participation Group, Harvard University, the Instituto de Astrofisica de Canarias, the Michigan State/Notre Dame/JINA Participation Group, Johns Hopkins University, Lawrence Berkeley National Laboratory, Max Planck Institute for Astrophysics, Max Planck Institute for Extraterrestrial Physics, New Mexico State University, New York University, Ohio State University, Pennsylvania State University, University of Portsmouth, Princeton University, the Spanish Participation Group, University of Tokyo, University of Utah, Vanderbilt University, University of Virginia, University of Washington, and Yale University.

APPENDIX

PHOTOMETRIC DISTANCE PDFS FOR GIANT STARS

In this appendix, we describe the calculation of the photometric-distance distributions $p(d|l, b, (J - K_s)_0, H_0, [\text{Fe}/\text{H}], \text{DF}, \text{iso})$ for the stars in our sample. The photometric-distance PDF for each star is the combination of the probability of its observed photometry, given a model for the color–absolute-magnitude distribution of giant stars, and a prior on the distance. Thus, we write

$$\begin{aligned} p(d|l, b, (J - K_s)_0, H_0, [\text{Fe}/\text{H}], \text{DF}, \text{iso}) &\propto p((J - K_s)_0, H_0|d, [\text{Fe}/\text{H}], \text{iso}) p(d, l, b|\text{DF}) \\ &= \text{iso}_{[\text{Fe}/\text{H}]}(H_0 - \mu(d), (J - K_s)_0) \nu_*(R, z|\text{DF}) d^2 \cos b, \end{aligned} \quad (\text{A1})$$

where μ is the distance modulus, and $d^2 \cos b$ is the Jacobian for the coordinate transformation $(R, \phi, z) \rightarrow (d, l, b)$, because we have anticipated that the distance prior is written in Galactocentric cylindrical coordinates (R, z, ϕ) . This prior is an exponential distribution in R , $\nu_*(R, z|\text{DF}) \propto \exp(-R/h_R)$; our sample is sufficiently close to the plane that vertical density gradients are unimportant (see FIG. 2). We have implicitly assumed that the prior does not depend on $[\text{Fe}/\text{H}]$. Our fiducial model has $h_R = 3$ kpc, as is appropriate for the metal-rich disk stars that make up our sample (Bovy et al. 2012c).

In Equation (A1), we have also anticipated that we obtain the probability of the observed photometry of the star, given its distance from a model for the isochrones of giants, combined with a model for the distribution along the isochrone from an initial-mass-function model; this probability is labeled as ‘iso’. We only use the color $(J - K_s)_0$ and the magnitude H_0 , as little is gained by adding J_0 or $K_{s,0}$ separately, and we compute the density in the color–absolute-magnitude plane for a given age and metallicity (which constitutes a single isochrone) by counting the number of stars generated from an initial mass function in small boxes in $(J - K_s)_0 - H_0$. For stars in our sample, we find the nearest Z/Z_\odot (assuming $Z_\odot = 0.019$) on a grid with a 0.0005 dex spacing, and we average Padova isochrones for metallicities $Z/Z_\odot, Z/Z_\odot - 0.0005$, and $Z/Z_\odot, +0.0005$, except at the edges of the grid at $Z/Z_\odot = 0.0005$ and $Z/Z_\odot = 0.03$. We average over age by assuming a constant star-formation rate up to 12 Gyr (except for the fit in § 4.2 with multiple populations, where we use an exponentially-declining star-formation rate). We use a lognormal Chabrier (2001) model for the IMF (but the resulting distance PDFs are essentially the same when using a Kroupa 2003 IMF). The resulting density for a star with solar metallicity is shown in FIG. 11. For a given distance and $[\text{Fe}/\text{H}]$, the probability of a star’s magnitude given its color is evaluated by computing its absolute magnitude M_H and evaluating a density like the one shown in FIG. 11.

The distribution $\text{iso}_{[\text{Fe}/\text{H}]}(H_0 - \mu(d), (J - K_s)_0)$ is relatively insensitive to changes in $[\text{Fe}/\text{H}]$ at high metallicity ($[\text{Fe}/\text{H}] \gtrsim -0.4$), where 90% of our sample lies. Thus, for the majority of the stars in our sample, the photometric distance PDF does not strongly depend on the measured $[\text{Fe}/\text{H}]$ and resembles FIG. 11.

Also shown in FIG. 11 is the direction that extinction moves objects in color and magnitude. In contrast to the case for the main sequence, this direction is at a large angle with the locus of the giant branch, such that under- or over-estimated extinction values can significantly change the photometric-distance PDF. The length of the extinction arrow in this figure is the median extinction in $(J - K_s)$ for the sample (0.45 mag).

ANALYSIS TESTS ON MOCK DATA SAMPLES

In this section, we perform extensive mock data analyses to test the methodology and approximations described in § 3, and to determine at what level the data are sensitive to changes in the Galactic parameters. We create mock data sets by re-sampling the line-of-sight velocity for each data point from its PDF $p(V_{\text{los}}|l, b, (J - K_s)_0, H_0, [\text{Fe}/\text{H}], \text{DF}, \text{iso})$.

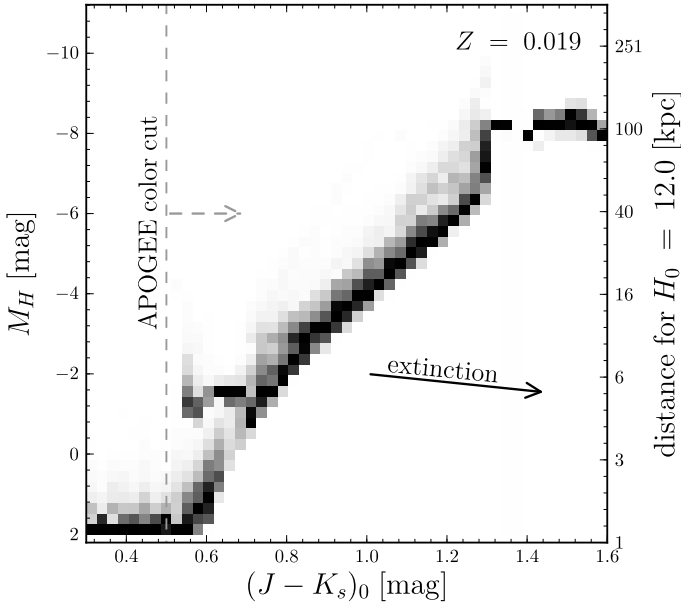


FIG. 11.— Density in the color–magnitude plane, for the giant branch of stars with solar metallicity. Each color bin is normalized separately to show the absolute-magnitude distribution at each color. This density is calculated using Padova isochrones (Bertelli et al. 1994; Bonatto et al. 2004; Marigo et al. 2008; Girardi et al. 2010), assuming a lognormal Chabrier (2001) IMF and a constant star-formation rate. This figure is an example of the density that we use as the photometric-distance distribution for each star. The length of the extinction arrow is the median extinction for the sample (0.45 in $J - K_s$).

TABLE 3
GALACTIC PARAMETERS FOR A FLAT-ROTATION-CURVE FIT TO MOCK DATA SETS

Parameter	Data / Mock input	Mock 1	Mock 2	Mock 3	Mock 4	Mock 5
$V_c(R_0)$ [km s $^{-1}$]	218 \pm 6	225 $^{+1}_{-10}$	222 \pm 5	221 $^{+1}_{-12}$	225 $^{+1}_{-11}$	217 $^{+1}_{-12}$
R_0 [kpc]	8.1 $^{+1.2}_{-0.1}$	8.0 $^{+1.2}_{-0.1}$	8.0 $^{+1.1}_{-0.1}$	7.9 $^{+0.9}_{-0.1}$	8.0 $^{+0.6}_{-0.1}$	7.8 $^{+0.9}_{-0.1}$
$V_{R,\odot}$ [km s $^{-1}$]	-10.5 $^{+0.5}_{-0.8}$	-10.3 $^{+0.8}_{-0.4}$	-9.3 $^{+0.6}_{-0.4}$	-9.8 $^{+1.0}_{-0.4}$	-10.8 $^{+0.9}_{-0.4}$	-9.4 $^{+0.9}_{-0.4}$
Ω_\odot [km s $^{-1}$ kpc $^{-1}$]	30.0 $^{+0.3}_{-3.3}$	30.7 $^{+0.4}_{-4.2}$	30.6 $^{+0.3}_{-3.2}$	30.3 $^{+0.4}_{-3.7}$	30.7 $^{+0.3}_{-2.5}$	30.3 $^{+0.4}_{-3.8}$
$\sigma_R(R_0)$ [km s $^{-1}$]	31.4 $^{+0.1}_{-3.2}$	32.0 $^{+0.2}_{-2.2}$	28.8 $^{+1.0}_{-0.6}$	31.5 $^{+1.0}_{-1.1}$	34.3 $^{+0.1}_{-3.1}$	29.3 $^{+1.8}_{-0.4}$
R_0/h_σ	0.03 $^{+0.1}_{-0.27}$	0.10 $^{+0.01}_{-0.17}$	-0.07 \pm 0.06	0.07 $^{+0.04}_{-0.09}$	0.25 $^{+0.01}_{-0.19}$	-0.04 $^{+0.08}_{-0.04}$
$X^2 \equiv \sigma_\phi^2/\sigma_R^2$	0.70 $^{+0.30}_{-0.01}$	0.38 $^{+0.21}_{-0.02}$	0.60 $^{+0.12}_{-0.03}$	0.39 $^{+0.13}_{-0.01}$	0.35 $^{+0.19}_{-0.02}$	0.50 $^{+0.09}_{-0.03}$
$\Delta\chi^2/\text{dof}$...	-0.19	-0.18	-0.20	-0.17	-0.22

NOTE. — The final line of this table has the difference in χ^2 per degree-of-freedom between the best-fit to the mock data set and the best-fit to the real data. Parameters are as in TABLE 2.

$(J - K_s)_0, H_0, [\text{Fe}/\text{H}], V_c(R), R_0, V_{R,\odot}, V_{\phi,\odot}, \text{DF, iso}$) (Equation (1)) in the best-fit model with a flat rotation curve for the real data (TABLE 2). However, rather than using the simple Gaussian-with-asymmetric-drift-offset model, we sample from a Dehnen distribution function (Equation (6)), with a radial scale length of $h_R = 3$ kpc, and a radial-velocity-dispersion scale length taken from the best-fit model. Because the Dehnen distribution function has X^2 built-in, we do not use the best-fit X^2 . For a Dehnen DF, the marginalization of the planar velocity distribution over the component of the velocity that is tangential to the line-of-sight cannot be done analytically, and we numerically integrate over this component. We do not add any observational error to the mock line-of-sight velocities, as the observational uncertainties are vanishingly small (see § 2). In this manner we produce five mock data sets that are exactly like the real data, except for the line-of-sight velocities.

We apply the exact same fitting procedure to the mock data as is used for the real data. We fit the five mock data sets with a flat-rotation curve model, and obtain the best-fits and uncertainties given in TABLE 3 (for comparison, this table also includes the best-fit model for the real data that was used to generate the mock data). We see that the true values for the parameters of interest are recovered well by the methodology of § 3. We also see that the uncertainty ranges on the Galactic parameters are similar, both in size and asymmetry, to those derived for the real data. Therefore, the best-fit parameters do not appear to be biased by the approximate methodology used in this paper, and the uncertainties are as should be expected from these mock data tests.

We also fit models with a non-flat rotation curve to the mock data sets. We only do this for three of the mock data

TABLE 4
GALACTIC PARAMETERS FOR NON-FLAT-ROTATION-CURVE FITS TO MOCK DATA SETS

Rotation curve	Parameter	Data / Mock input	Mock 1	Mock 2	Mock 3
power-law	$V_c(R_0)$ [km s $^{-1}$]	218 \pm 6	224 $^{+28}_{-2}$	222 $^{+8}_{-21}$	224 $^{+4}_{-27}$
	β	...	0.07 $^{+0.06}_{-0.04}$	0.02 $^{+0.02}_{-0.11}$	0.08 $^{+0.01}_{-0.14}$
	R_0 [kpc]	8.1 $^{+1.2}_{-0.1}$	8.0 $^{+1.2}_{-0.1}$	8.0 $^{+0.7}_{-0.1}$	8.0 $^{+0.7}_{-0.1}$
	$V_{R,\odot}$ [km s $^{-1}$]	-10.5 $^{+0.5}_{-0.8}$	-9.7 $^{+0.7}_{-0.4}$	-9.3 $^{+0.5}_{-0.7}$	-9.1 $^{+0.7}_{-0.6}$
	Ω_\odot [km s $^{-1}$ kpc $^{-1}$]	30.0 $^{+0.3}_{-3.3}$	30.8 $^{+0.5}_{-2.2}$	30.4 $^{+0.2}_{-3.9}$	30.5 $^{+0.5}_{-4.6}$
	$\sigma_R(R_0)$ [km s $^{-1}$]	31.4 $^{+0.1}_{-3.2}$	31.8 $^{+0.2}_{-2.2}$	29.4 \pm 1.0	33.3 $^{+0.4}_{-1.6}$
	R_0/h_σ	0.03 $^{+0.01}_{-0.27}$	0.07 $^{+0.01}_{-0.14}$	-0.05 $^{+0.05}_{-0.08}$	0.17 $^{+0.04}_{-0.11}$
	$X^2 \equiv \sigma_\phi^2/\sigma_R^2$	0.70 $^{+0.30}_{-0.01}$	0.44 $^{+0.16}_{-0.01}$	0.59 $^{+0.10}_{-0.04}$	0.36 $^{+0.09}_{-0.02}$
linear	$V_c(R_0)$ [km s $^{-1}$]	218 \pm 6	223 \pm 12	222 $^{+20}_{-11}$	224 $^{+11}_{-32}$
	$dV_c/dR(R_0)$ [km s $^{-1}$ kpc $^{-1}$]	...	2.0 $^{+0.8}_{-2.7}$	1 $^{+1}_{-3}$	2.8 $^{+0.8}_{-5.2}$
	R_0 [kpc]	8.1 $^{+1.2}_{-0.1}$	8.0 $^{+1.0}_{-0.1}$	8.0 $^{+0.8}_{-0.1}$	8.0 $^{+0.8}_{-0.1}$
	$V_{R,\odot}$ [km s $^{-1}$]	-10.5 $^{+0.5}_{-0.8}$	-9.7 \pm 0.7	-9.1 $^{+0.9}_{-0.2}$	-8.9 \pm 0.6
	Ω_\odot [km s $^{-1}$ kpc $^{-1}$]	30.0 $^{+0.3}_{-3.3}$	30.8 $^{+0.3}_{-4.3}$	31 $^{+1}_{-3}$	30.6 $^{+0.3}_{-5.8}$
	$\sigma_R(R_0)$ [km s $^{-1}$]	31.4 $^{+0.1}_{-3.2}$	31.3 $^{+0.5}_{-1.6}$	30.0 $^{+0.2}_{-2.1}$	32.8 $^{+0.6}_{-1.7}$
	R_0/h_σ	0.03 $^{+0.01}_{-0.27}$	0.04 $^{+0.03}_{-0.09}$	-0.03 $^{+0.01}_{-0.13}$	0.12 $^{+0.02}_{-0.10}$
	$X^2 \equiv \sigma_\phi^2/\sigma_R^2$	0.70 $^{+0.30}_{-0.01}$	0.46 $^{+0.13}_{-0.03}$	0.59 $^{+0.14}_{-0.01}$	0.40 $^{+0.13}_{-0.02}$
cubic	$V_c(R_0)$ [km s $^{-1}$]	218 \pm 6	223 $^{+21}_{-3}$	223 $^{+11}_{-5}$	223 $^{+16}_{-6}$
	$dV_c/dR(R_0)$ [km s $^{-1}$ kpc $^{-1}$]	...	2.6 $^{+0.6}_{-1.9}$	-1 \pm 1	1 \pm 1
	$d^2V_c/dR^2(R_0)$ [km s $^{-1}$ kpc $^{-2}$]	...	-0.2 $^{+0.1}_{-0.2}$	0.1 $^{+0.1}_{-0.3}$	-0.3 $^{+0.3}_{-0.1}$
	$d^3V_c/dR^3(R_0)$ [km s $^{-1}$ kpc $^{-3}$]	...	0.002 $^{+0.040}_{-0.007}$	0.05 $^{+0.04}_{-0.01}$	0.08 \pm 0.02
	R_0 [kpc]	8.1 $^{+1.2}_{-0.1}$	8.0 $^{+1.2}_{-0.1}$	8.1 $^{+0.9}_{-0.1}$	8.0 $^{+0.8}_{-0.1}$
	$V_{R,\odot}$ [km s $^{-1}$]	-10.5 $^{+0.5}_{-0.8}$	-9.3 $^{+0.2}_{-0.7}$	-9.6 $^{+0.8}_{-0.5}$	-9.2 $^{+0.3}_{-0.7}$
	Ω_\odot [km s $^{-1}$ kpc $^{-1}$]	30.0 $^{+0.3}_{-3.3}$	30.6 $^{+0.3}_{-2.7}$	30.7 $^{+0.3}_{-2.9}$	30.3 $^{+0.5}_{-2.4}$
	$\sigma_R(R_0)$ [km s $^{-1}$]	31.4 $^{+0.1}_{-3.2}$	32.6 $^{+0.2}_{-2.0}$	28.6 $^{+0.8}_{-0.7}$	33.0 $^{+0.3}_{-1.3}$
	R_0/h_σ	0.03 $^{+0.01}_{-0.27}$	0.11 $^{+0.03}_{-0.10}$	-0.12 $^{+0.05}_{-0.08}$	0.13 $^{+0.06}_{-0.07}$
	$X^2 \equiv \sigma_\phi^2/\sigma_R^2$	0.70 $^{+0.30}_{-0.01}$	0.42 $^{+0.12}_{-0.02}$	0.62 \pm 0.05	0.35 $^{+0.07}_{-0.02}$

NOTE. — Parameters in this table are as in TABLE 2.

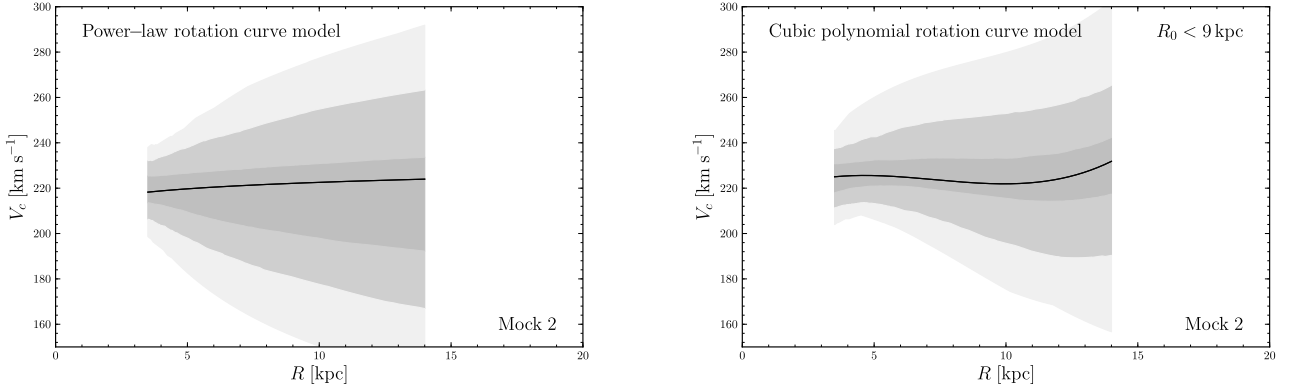


FIG. 12.— Same as FIG. 6, but for mock data set 2. To completely mimic the procedure applied to the real data we have imposed a $R_0 < 9$ kpc prior for the cubic-polynomial fit to the rotation curve, even though this only excludes tens of the 10,000 points that were sampled from the PDF (see TABLE 4).

sets; the results for fitting a power-law rotation curve, or a linear or cubic polynomial curve, are given in TABLE 4. We see that, in these cases, the Galactic parameters are recovered within the uncertainties, with perhaps a slight bias of a few km s $^{-1}$ in the best-fit parameters, although the (asymmetric) PDFs for the best-fit parameters do contain the “true” values within the 68% confidence intervals given. Again, the size of the uncertainties on the best-fit parameters for the mock data are similar to those found for the real data in TABLE 2.

In FIG. 12, we show for one of the mock data sets the same representation of the constraints on the shape of the rotation curve as is given for the real data in FIG. 6. Comparing these two figures, we see that the constraints are similar, with the real data giving a slightly narrower range around the best-fit, which is approximately flat. It is clear

that around $R = 14$ kpc, the constraints on the rotation curve from the current APOGEE data become weak, so we limit our discussion to $4 \text{ kpc} < R < 14 \text{ kpc}$ in this paper.

REFERENCES

Allende Prieto, C., Barklem, P. S., Lambert, D. L., & Cunha, K. 2004, *A&A*, 420, 183

Aumer, M. & Binney, J. J. 2009, *MNRAS*, 397, 1286

Bensby, T., Oey, M. S., Feltzing, S., & Gustafsson, B. 2007, *ApJ*, 655, 89

Bertelli, G., Bressan, A., Chiosi, C., Fagotto, F., & Nasi, E. 1994, *A&AS*, 106, 275

Binney, J., Gerhard, O. E., Stark, A. A., Bally, J., & Uchida, K. I. 1991, *MNRAS*, 252, 210

Binney, J. & Tremaine, S. 2008, *Galactic Dynamics: Second Edition* (Princeton University Press)

Blitz, L. & Spergel, D. N. 1991, *ApJ*, 379, 631

Bonatto, C., Bica, E., & Girardi, L. 2004, *A&A*, 415, 571

Bovy, J., Hogg, D. W., & Rix, H.-W. 2009a, *ApJ*, 704, 1704

Bovy, J., Hogg, D. W., & Roweis, S. T. 2009b, *ApJ*, 700, 1794

Bovy, J. 2010, *ApJ*, 725, 1676

Bovy, J. & Hogg, D. W. 2010, *ApJ*, 717, 617

Bovy, J., Rix, H.-W., & Hogg, D. W. 2012a, *ApJ*, 751, 131

Bovy, J., Rix, H.-W., Hogg, D. W., Beers, T. C., Lee, Y. S., & Zhang, L. 2012b, *ApJ*, 755, 115

Bovy, J., Rix, H.-W., Liu, C., Hogg, D. W., Beers, T. C., & Lee, Y. S. 2012c, *ApJ*, 753, 148

Bovy, J. & Tremaine, S. 2012, *ApJ*, 756, 89

Carignan, C., Chemin, L., Huchtmeier, W. K., & Lockman, F. 2006, *ApJ*, 641, L109

Carlén, J. L., Majewski, S. R., Caselli-Dinescu, D. I., et al. 2012, *ApJ*, 744, 25

Carpenter, J. M. 2001, *AJ*, 121, 2851

Casagrande, L., Schöönrich, R., Asplund, M., et al. 2011, *A&A*, 530, 138

Chabrier, G. 2001, *ApJ*, 554, 1274

Churchwell, E., Babler, B. L., Meade, M. R., et al. 2009, *PASP*, 121, 213

Clemens, D. P. 1985, *ApJ*, 295, 422

Dehnen, W. 1998, *AJ*, 115, 2384

Dehnen, W. & Binney, J. J. 1998, *MNRAS*, 298, 387

Dehnen, W. 1999, *AJ*, 118, 1201

Dehnen, W. 2000, *AJ*, 119, 800

Drimmel, R. & Spergel, D. N. 2001, *ApJ*, 556, 181

Eggen, O. J. 1986, *AJ*, 92, 910

Eisenstein, D., et al. 2011, *AJ*, 142, 72

Famaey, B., Siebert, A., & Jorissen, A. 2008, *A&A*, 483, 453

Feast, M. & Whitelock, P. 1998, *MNRAS*, 291, 683

Fich, M. & Tremaine, S. 1991, *ARA&A*, 29, 409

Flynn, C., Holmberg, J., Portinari, L., Fuchs, B., & Jahreiß, H. 2006, *MNRAS*, 372, 1149

Foreman-Mackey, D., Hogg, D. W., Lang, D., & Goodman, J. 2012, arXiv:1202.3665v2 [astro-ph.IM]

Freeman, K. C. 1987, *ARA&A*, 25, 603

Frinchaboy, P. M. 2008, Ph.D. thesis, Univ. Virginia

Ghez, A. M., Salim, S., Weinberg, N. N., et al. 2008, *ApJ*, 689, 1044

Gillessen, S., Eisenhauer, F., Trippe, S., Alexander, T., Genzel, R., Martins, F., Ott, T. 2009, *ApJ*, 692, 1075

Girardi, L., Groenewegen, M. A. T., Hatziminaoglou, E., da Costa, L. 2005, *A&A*, 436, 895

Girardi, L., Williams, B. F., Gilbert, K. M., et al. 2010, *ApJ*, 724, 1030

Gunn, J. E., Knapp, G. R., & Tremaine, S. D. 1979, *AJ*, 84, 1181

Gunn, J. E., et al. 2006, *AJ*, 131, 2332

Hammer, F., Puech, M., Chemin, L., Flores, H., & Lehnert, M. D. 2007, *ApJ*, 662, 322

Hogg, D. W., Blanton, M. R., Roweis, S. T., & Johnston, K. V. 2005, *ApJ*, 629, 268

Jackson, P. D. & Kerr, F. J. 1981, *BAAS*, 13, 538

Jackson, P. D. 1985, in *The Milky Way Galaxy, Proceedings of IAU Symposium No. 106*, eds. H. van Woerden, R. J. Allen, and W. B. Burton (Dordrecht: D. Reidel Publishing Co.), 179

Kapteyn, J. C. 1905, *Br. Assoc. Adv. Sci. Rep. A*, 257

Kerr, F. J. 1962, *MNRAS*, 123, 327

Kerr, F. J. & Lynden-Bell, D. 1986, *MNRAS*, 221, 1023

Klypin, A., Zhao, H., & Somerville, R. S. 2002, *ApJ*, 573, 597

Knapp, G. R., Tremaine, S. D., & Gunn, J. E. 1979, *AJ*, 83, 1585

Koposov, S. E., Rix, H.-W., & Hogg, D. W. 2010, *ApJ*, 712, 260

Kroupa, P. 2003, *MNRAS*, 322, 231

Kuijken, K. & Tremaine, S. 1991, in *Dynamics of Disk Galaxies*, ed. B. Sundelius (Göteborg: Göteborg Univ. Press), 257

Kuijken, K. & Tremaine, S. 1994, *ApJ*, 421, 178

Kurucz, R. L. 1979, *ApJS*, 40, 1

Law, D. R., Majewski, S. R., & Johnston, K. V. 2009, *ApJ*, 703, 67

Levine, E. S., Heiles, C., & Blitz, L. 2008, *ApJ*, 679, 1288

Lewis, J. R., & Freeman, K. C. 1989, *AJ*, 97, 139

Lin, C. C., Yuan, C., & Shu, F. H. 1969, *ApJ*, 155, 721

Majewski, S. R., Law, D. R., Polak, A. A., Patterson, R. J. 2006, *ApJ*, 637L, 25

Majewski, S. R., Zasowski, G., Nidever, D. L. 2011, *ApJ*, 739, 25

Mario, P., Girardi, L., Bressan, A., Groenewegen, M. A. T., Silva, L., & Granato, G. L. 2008, *A&A*, 482, 883

McMillan, P. J. & Binney, J. J. 2010, *MNRAS*, 402, 934

Merrifield, M. R. 1992, *AJ*, 103, 1552

Navarro, J. F., Frenk, C. S., & White, S. D. M. 1997, *ApJ*, 490, 493

Pietrinferni, A., Cassisi, S., Salaris, M., & Castelli, F. 2004, *ApJ*, 612, 168

Reid, M. J. & Brunthaler, A. 2004, *ApJ*, 616, 872

Reid, M. J., Menten, K. M., Zheng, X. W., et al. 2009, *ApJ*, 700, 137

Schöönrich, R., Binney, J. J., & Dehnen, W. 2010, *MNRAS*, 403, 1829

Schöönrich, R. 2012, *MNRAS*, in press, arXiv:1207.3079

Schwarzschild, K. 1907, *Nachr. Koniglichen Ges. Wiss. Goett.*, 5, 614

Sellwood, J. A. 2010, *MNRAS*, 409, 145

Shuter, W. L. H. 1982, *MNRAS*, 199, 109

Siebert, A., Famaey, B., Minchev, I., et al. 2011, *MNRAS*, 412, 2026

Sirk, E., Goodman, J., Knapp, G. R., Brinkmann, J., Ivezić, Z., Knerr, E. J., Schlegel, D. J., Schneider, D. P., & York, D. G. 2004, *AJ*, 127, 914

Skrutskie, M. F., Cutri, R. M., Stiening, R., et al. 2006, *AJ*, 131, 1163

Strömborg, G. 1946, *ApJ*, 104, 12

Toomre, A. 1964, *ApJ*, 139, 1217

van de Hulst, H. C., Muller, C. A., & Oort, J. H. 1954, *BAN*, 12, 117

van der Marel, R. P., Fardal, M., Besla, G., Beaton, R. L., Sohn, S. T., Anderson, J., Brown, T., & Guhathakurta, P. 2012, *ApJ*, 753, 8

Watkins, L. L., Evans, N. W., An, J. H. 2010, *MNRAS*, 406, 264

Wielen, R., Fuchs, B., & Dettbarn, C. 1996, *A&A*, 314, 438

Wilson, J. C., Hearty, F., Skrutskie, M. F., et al. 2010, *Proc. SPIE*, 7735, 46

Woltjer, L. 1975, *A&A*, 42, 109

Wright, E. L., Eisenhardt, P. R. M., Mainzer, A. K., et al. 2010, *AJ*, 140, 1868

Xue, X. X., Rix, H.-W., Zhao, G., et al. 2008, *ApJ*, 684, 1143

Zasowski, G., Majewski, S. R., Indebetouw, R., et al. 2009, *ApJ*, 707, 510